

AN INCLUSIVE SEARCH FOR LONG-LIVED
DECAYS WITH THE CMS DETECTOR AT THE
LARGE HADRON COLLIDER IN $\sqrt{s} = 13$ TEV
DATA

JOSHUA ROBERT HARDENBROOK

A DISSERTATION
PRESENTED TO THE FACULTY
OF PRINCETON UNIVERSITY
IN CANDIDACY FOR THE DEGREE
OF DOCTOR OF PHILOSOPHY

RECOMMENDED FOR ACCEPTANCE
BY THE DEPARTMENT OF
PHYSICS
ADVISER: CHRISTOPHER G. TULLY

2017

© Copyright by Joshua Robert Hardenbrook, 2017.

All rights reserved.

Abstract

A search for long-lived particles decaying to jets is presented, performed on the data collected by CMS at a center-of-mass energy $\sqrt{s} = 13$ TeV in 2015. The data set corresponds to an integrated luminosity of 2.7 fb^{-1} . The analysis exploits a set of trigger algorithms and a customized displaced-jet tagger. The number of tagged displaced-jets is used to characterize a potential signal. The pair production of long-lived particles decaying to two jets or to a b jet and a lepton is excluded for masses lighter than 450–1000 GeV, for lifetimes between 1 mm to 1 m.

Acknowledgements

This is where I acknowledge peeeeeepople

This is the dedication all about how my thesis got turned right upside down

Contents

Abstract	iii
Acknowledgements	iv
1 Introduction	1
1.1 The Standard Model	1
1.2 Beyond The Standard Model	1
2 Experimental Setup	2
2.1 Founding and History	2
2.2 Large Hadron Collider	2
2.3 Other LHC Related Experiments	3
2.4 Compact Muon Solenoid Experiment	3
2.4.1 ECAL	5
2.4.2 HCAL	5
2.4.3 Tracking	5
2.4.4 Muon Chambers	5
2.4.5 Trigger System	5
3 Theory	9
3.1 Standard Model of Particle Physics	9
3.1.1 Quantum Field Theory	9
3.1.2 Symmetries in the Standard Model	9

3.1.3	Fundamental Fields of the Standard Model Lagrangian	10
3.1.4	Sectors of the Standard Model Lagrangian	10
3.1.5	Electroweak Symmetry Breaking	12
3.1.6	The Narrow Width Approximation	12
3.2	Supersymmetry	12
3.2.1	Electroweak Symmetry Breaking in Supersymmetric Theories	12
3.3	Origins of Long-lived Signatures	12
3.3.1	Standard Model Particles with Long Lifetimes	12
3.3.2	Split-Susy and Naturalness at the LHC	13
4	Strategies for Discovering New Physics at the LHC	16
5	Displaced Jet Analysis	17
5.1	Introduction	17
5.2	Datasets	18
5.3	Coordinate Conventions	18
5.4	An inclusive displaced-jet tagger	20
5.5	Event selection	20
5.6	Datasets and simulated samples	21
5.7	Background prediction	22
5.7.1	Signal Injection Tests	25
5.7.2	Tag Probability Cross Validation	31
5.8	Systematic uncertainties	35
5.8.1	Background systematic uncertainties	35
5.8.2	Signal systematic uncertainties	35
5.9	Results and interpretation	38
Bibliography		52

Chapter 1

Introduction

1.1 The Standard Model

Standard model things [1]

1.2 Beyond The Standard Model

Chapter 2

Experimental Setup

2.1 Founding and History

2.2 Large Hadron Collider

The bunches of protons in the LHC are bent into a circular trajectory by more than 1200 superconducting dipole magnets and are focused and maintained close to the ideal orbit around the ring by hundreds of superconducting quadrupole magnets. Thousands of corrector magnets around the ring allow the beam to be steered closer

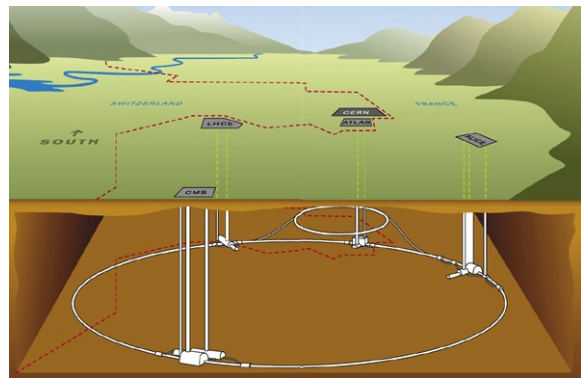


Figure 2.1: The LHC tunnel installed on the border of Geneva, Switzerland and France. The experiments are distributed along the circumference of the ring.

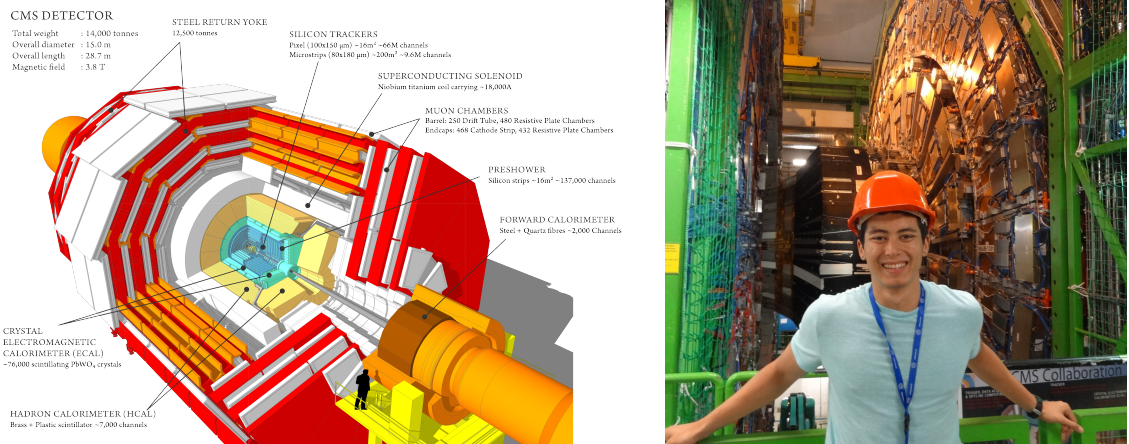


Figure 2.2: (left) A tear-away view of the inner detectors of CMS. (right) The CMS endcap currently detached from the inner barrel for upgrades during the shutdown.

to the ideal orbit, make the focusing independent of the particles' energy variations within a bunch, and cancel the effects of higher order multipoles in the fields induced by small field imperfections in the main magnets. The radiofrequency (RF) field in superconducting cavities is placed periodically around the ring and accelerates the protons from the injection energy of 450 GeV to the final operating energy, which is designed to be 7 TeV per beam. The RF field also causes the protons to be bunched, as only particles at or near a certain "equilibrium phase" on the RF wave will be accelerated stably. Special quadrupoles around each interaction region focus the bunches down to a small transverse size, to increase the likelihood of a proton-proton collision each time two bunches pass through each other.

2.3 Other LHC Related Experiments

2.4 Compact Muon Solenoid Experiment

The Compact Muon Solenoid (CMS) Detector is a general-purpose detector consisting of an all silicon tracker, a precision electromagnetic calorimeter (ECAL), a

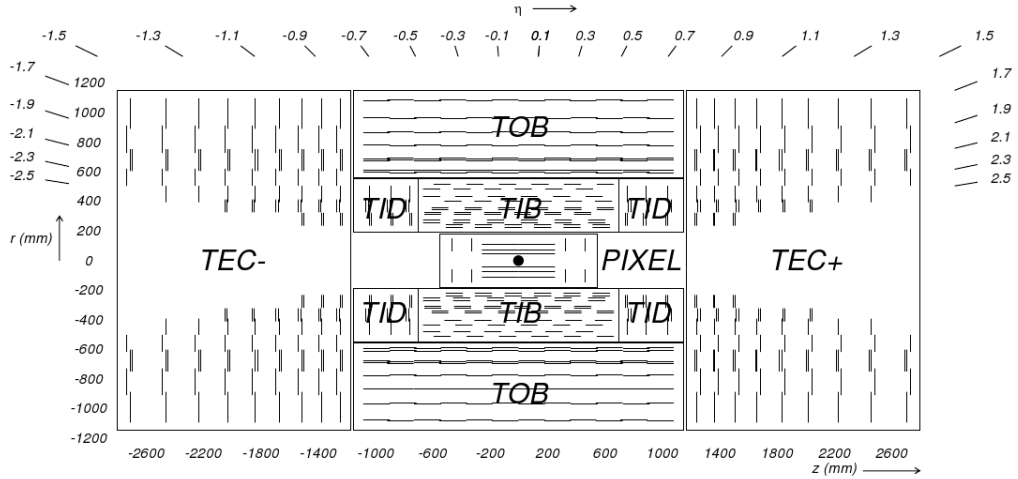


Figure 2.3: The CMS Tracker

hadron calorimeter (HCAL), a 4 T superconducting solenoid and muon chambers. The solenoid deflects charged particles whose paths are traced in the tracker, making it possible to reconstruct the particles' momentum. The two calorimeters reconstruct the energy of and identify photons, electrons and hadronic jets. As shown in Figure 2.2 the detector has cylindrical symmetry about the interaction point where the proton beams collide. By maintaining near full coverage of the interaction point it is possible to detect signatures such as neutrinos or other weakly interacting particles as missing energy.

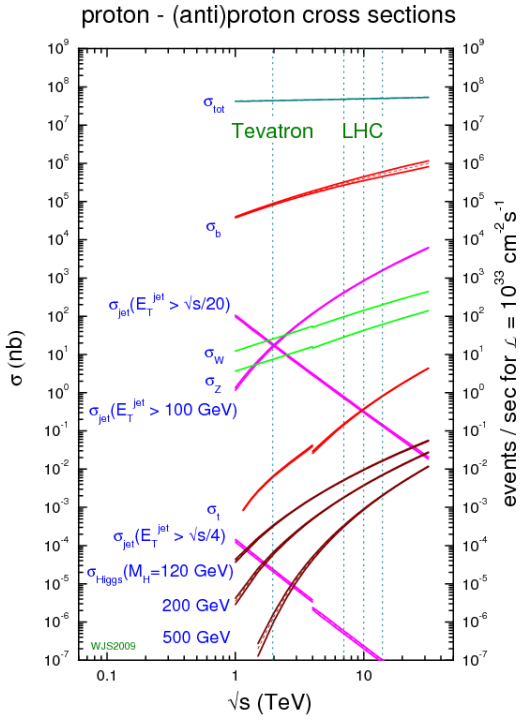


Figure 2.4: Common cross sections of proton collisions as a function of the center of mass energy \sqrt{s}

2.4.1 ECAL

2.4.2 HCAL

2.4.3 Tracking

2.4.4 Muon Chambers

2.4.5 Trigger System

The CMS Trigger System exists as a filter through which events are determined to be “interesting”. It is both unnecessary and inefficient to record anything that occurs in the detector electronics. Most events that occur from colliding protons are well understood. To the left, you can see the logarithmic plot of common physics

processes for proton-proton scattering. Events such as the production of a b quark occur at $\approx 10^6$ Hz at a luminosity of $\mathcal{L} = 10^{33}$ cm $^{-2}$ whereas the production of the Higgs is much lower at $\approx 10^{-2}$ Hz.

At design luminosity, the LHC has beam crossings at a rate of ≈ 40 MHz with each crossing coming spaced at ≈ 25 ns. For each crossing there are ≈ 20 inelastic collisions (referred to as pile up) contained in an event file of ≈ 1 Mb. However the bandwidth for storage is limited to $\approx 10^2$ Hz and equivalently 10² Mb/s. Generally, all but one of the inelastic collisions is interesting and a large excess of uninteresting activity is generated in the detector electronics. The trigger must be robust enough to select this needle in a haystack event while remaining computationally efficient in maximizing the limited bandwidth.

The CMS Trigger system is designed to read events at the event crossing frequency and generate the factor 10⁵ of rejection between the crossing frequency and the archival capacity. This factor is far too large to achieve in a single step given the complexity of triggers and event reconstruction. Therefore the task is split into two steps: The Level 1 (L1) and High Level (HLT) Trigger systems.

The $O(10^7)$ events per second first pass through the L1 Trigger which reads out events at 10⁵ Hz. From here, the High Level Trigger makes the final decision as to which events are kept. Approximately 350 Hz is processed and stored, 300 Hz is “parked” (stored but processed later), and 1 kHz is partially stored (only the HLT level information and not the RAW detector information) and used for data scouting for future analysis.

The most basic criterion for interesting events are hard physics events with high momentum transfer, q^2 . As the protons collide with effectively no transverse

momentum, any event with significant deposits of transverse energy (or even missing transverse momentum) is indicative of a hard physics process. The number of objects with a given transverse momentum falls off exponentially, so a simple minded way to reduce the rate of processed events is to raise the threshold of accepted events.

More specific criterion for “interesting events” is analysis dependent. Generally, analyses are categorized by their final state signature. Thus, the trigger requires loose identification on the objects of that signature such as the isolation and shape of energy deposition. Once the event has passed the Level 1 and HLT Triggers, tighter and more computationally costly selection can be made offline where we are unrestricted by bandwidth limitations.

As there is a limited amount of bandwidth for processing the events, the numerous analyses of CMS are given a budget (measured in Hz) for the triggers they request. As it stands the $H \rightarrow \gamma\gamma$ analysis is assigned a budget of 30 Hz for its diphoton trigger suite. As the diphoton channel was of high priority in the 7 and 8 TeV running this accounted for a significant fraction ($\approx 10\%$) of the overall budget.

As the luminosity of the machine increases, we expect proportionally more events per second and must accordingly alter the triggers.

Level 1 (L1) Trigger

High Level Trigger (HLT)

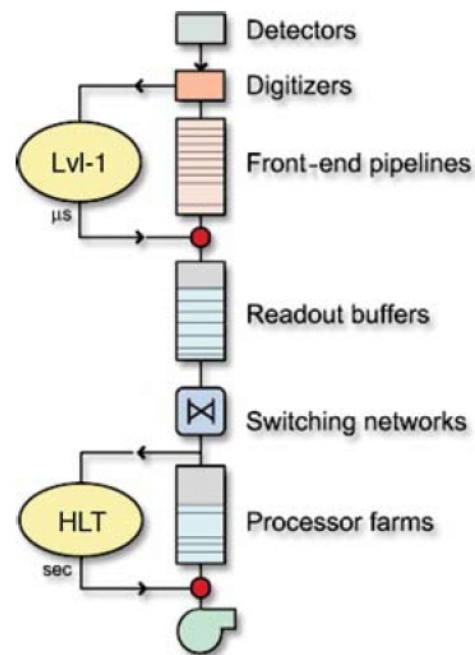


Figure 2.5: A diagrammatic representation of the level 1 and HLT trigger processing

Chapter 3

Theory

3.1 Standard Model of Particle Physics

3.1.1 Quantum Field Theory

In classical lagrangian kinematics, the time evolution of some coordinate q is determined via the principle of minimal action.

$$S[q(t)] = \int_{t_1}^{t_2} L(q, \frac{dq}{dt}, t) dt \quad (3.1)$$

where S is a functional of the time dependent coordinate $q(t)$.

3.1.2 Symmetries in the Standard Model

The fundamental forces and their interactions arise from the symmetries preserved by the standard model lagrangian.

3.1.3 Fundamental Fields of the Standard Model Lagrangian

3.1.4 Sectors of the Standard Model Lagrangian

The Standard Model of particle physics consists of a quantum field theory lagrangian with four sectors:

$$\mathcal{L}_{SM} = \mathcal{L}_{Gauge} + \mathcal{L}_{Fermion} + \mathcal{L}_{Higgs} + \mathcal{L}_{Yukawa} \quad (3.2)$$

and three gauge group symmetries: $U(1)_Y$ hypercharge, $SU(2)_L$ left chiral and $SU(3)_c$ color. All standard model particles transform as a multiplet of $SU(3) \times SU(2)_L \times U(1)_Y$.

The gauge sector consists of the field stress energy tensor of the 3 corresponding types of gauge bosons: G^i (gluons of the color force), W^i (W 's of the weak force) and B (B 's of the weak hypercharge). Here the index i enumerates their multiplicity. There are 8 gluons, 3 W 's and a single B .

$$\mathcal{L}_{Gauge} = -\frac{1}{4}F_{\mu\nu}^i F^{\mu\nu i} = -\frac{1}{4}G_{\mu\nu}^i G^{\mu\nu i} - \frac{1}{4}W_{\mu\nu}^i W^{\mu\nu i} - \frac{1}{4}B_{\mu\nu} B^{\mu\nu} \quad (3.3)$$

where the double scripts correspond to the antisymmetric commutator, that is:

$$X_{\mu\nu}^i = [D_{[\mu} X_{\nu]}^i] = D_\mu X_\nu^i - D_\nu X_\mu^i - g f_{ijk} X_\mu^j X_\nu^k \quad (3.4)$$

where the D_μ terms correspond to the covariant derivative and the f_{ijk} are the corresponding structure constants for the algebra. and g the coupling constant. In full, the field stress tensor terms are:

$$\begin{aligned}
G_{\mu\nu}^i &= D_\mu G_\nu^i - D_\nu G_\mu^i - g_s f_{ijk} G_\mu^j G_\nu^k \\
W_{\mu\nu}^i &= D_\mu W_\nu^i - D_\nu W_\mu^i - g \epsilon_{ijk} W_\mu^j W_\nu^k \\
B_{\mu\nu}^i &= D_\mu B_\nu^i - D_\nu B_\mu^i
\end{aligned}$$

The fermion sector consists of the kinetic energy terms for each quark (up and down types) and leptons (lepton, neutrinos) in the standard model. The left handed quarks transform as an SU(2) doublet:

$$q_{mL\alpha}^0 = \begin{pmatrix} u_{m\alpha}^0 \\ d_{m\alpha}^0 \end{pmatrix}_L \quad (3.5)$$

where the subscript m denotes the family (1st, 2nd and 3rd generation) and α denotes the color charge (red, green, and blue).

$$l_{mL} = \begin{pmatrix} \nu_m^0 \\ e_m^{-,0} \end{pmatrix}_L \quad (3.6)$$

As the $SU(2)_L$ symmetry only acts on the left handed fermions we further separate the fermion sector into left and right components:

$$\mathcal{L}_{fermion,L} = \bar{q}_{mL}^0 i\gamma^\mu D_\mu q_{mL}^0 + \bar{l}_{mL}^0 i\gamma^\mu D_\mu l_{mL}^0 \quad (3.7)$$

$$\mathcal{L}_{fermion,R} = \bar{u}_{mR}^0 i\gamma^\mu D_\mu u_{mR}^0 + \bar{d}_{mR}^0 i\gamma^\mu D_\mu d_{mR}^0 + \bar{e}_{mR}^0 i\gamma^\mu D_\mu e_{mR}^0 + \bar{\nu}_{mR}^0 i\gamma^\mu D_\mu \nu_{mR}^0 \quad (3.8)$$

The higgs sector consists of terms related to the single scalar field ϕ

3.1.5 Electroweak Symmetry Breaking

3.1.6 The Narrow Width Approximation

3.2 Supersymmetry

3.2.1 Electroweak Symmetry Breaking in Supersymmetric Theories

3.3 Origins of Long-lived Signatures

3.3.1 Standard Model Particles with Long Lifetimes

The standard model already includes a variety of particles that can generate displaced vertices (Table 3.1 Table 3.2). For example, $B^0 \rightarrow J/\psi K^{*0}$ with $K^{*0} \rightarrow K^+ \pi^-$ generates a 4 track vertex. Such a vertex is commonly utilized in b-tagging. Of particular interest to single displaced jet identification outside of the b-tagging regime are charge neutral SM particles decaying to charged particles with a few centimeter lifetime: Λ^0 , K_S^0 . Such particles would have no track leading to the primary vertex and vertices far outside the b lifetime. The most relevant of processes being:

1. $K_s^0 \rightarrow \pi^+ \pi^-$ 69% of all K_s^0 decays
2. $\Lambda^0 \rightarrow p \pi^-$ 64% of all Λ^0 decays

Jets containing prompt and non-prompt K_s and Λ^0 will contain tracks with large impact parameters, and large impact parameter significance. When a vertex is fit to the matched tracks we expect small track multiplicity relative to the GeV to TeV long-lived particles this identification targets. It is important to separate this contribution from the detector effects like nuclear interactions.

Name	Content	Particle	mass (MeV)	τ_0 (sec)	$c\tau$ (cm)
Pion	ud	π^\pm	139	2.6×10^{-8}	7.8×10^2
Kaon	$u\bar{s}$	K^\pm	497	1.23×10^{-8}	3.7×10^2
K Short	$\frac{1}{\sqrt{2}}(d\bar{s} - s\bar{d})$	K_s^0	497	0.896×10^{-10}	2.68
K Long	$\frac{1}{\sqrt{2}}(d\bar{s} + s\bar{d})$	K_L^0	497	5.1×10^{-8}	1.5×10^3
D	cd	D^\pm	1869	1×10^{-12}	3.0×10^{-2}
B meson	ub	B^\pm	5279	1.6×10^{-12}	4.8×10^{-2}
strange B	$s\bar{b}$	B_s^0	5366	1.5×10^{-12}	4.5×10^{-2}
charmed B	$c\bar{b}$	B_c^0	6275	4.5×10^{-13}	1.4×10^{-2}

Table 3.1: Mesons with Lifetimes greater than 10^{-2} cm

Name	Content	Particle	mass [MeV]	τ_0 [s]	$c\tau_0$ [cm]
Lambda	uds	Λ^0	1115	2.6×10^{-10}	7.8
bottom Lambda	udb	Λ_b^0	5620	1.4×10^{-12}	4.2×10^{-2}
Sigma plus	uus	Σ^+	1189	8×10^{-11}	2.4
Sigma minus	dds	Σ^-	1197	1.4×10^{-10}	4.2
Xi zero	uss	Ξ^0	1314	4×10^{-13}	1.2×10^{-2}
Xi minus	dss	Ξ^-	1321	1.6×10^{-10}	4.8
charmed Xi +	usc	Ξ_c^+	2467	4.42×10^{-13}	1.3×10^{-2}
charmed Xi	dsc	Ξ_c^0	2471	1.12×10^{-13}	3.3×10^{-2}
bottom Xi	dsb	Ξ_b^-	5792	1.56×10^{-12}	4.7×10^{-2}
bottom Omega	ssb	Ω_b^-	6054	1.13×10^{-12}	3.3×10^{-2}
Omega minus	sss	Ω^-	1672	8×10^{-11}	2.4

Table 3.2: Baryons with Lifetimes greater than 10^{-2} cm

Particles of a characteristic lifetime τ decay with a falling exponential. For reference, a table describing the percent of decays that will occur at various distances is shown in Table 3.3. Even lifetimes 10 and 100 times the size of the tracker, we would still expect 10% and 1% respectively to occur within the tracker. For particles of lifetime λ we expect 0.6% to decay beyond 5λ .

3.3.2 Split-Susy and Naturalness at the LHC

The expectation of discovering supersymmetry (SUSY) at the TeV scale has been largely motivated by arguments based on naturalness. Since the mass of the Stan-

Distance (λ)	Probability of Decay
0.01	1%
0.1	9.5%
0.25	22%
0.5	39%
0.75	52%
1	63%
1.5	77%
2	86%
3	95%
5	99.3%

Table 3.3: A reference table for the cumulative probability for a particle of lifetime λ to have decayed after a given distance. Distance is in multiples of lambda.

standard Model Higgs boson is sensitive to the high energy scale where SUSY is broken (m_{SUSY}), its mass, of order the electroweak scale, ($m_h \approx m_{EW} \ll m_{SUSY}$) would need to be tuned to order m_{EW}^2/m_{SUSY}^2 . To avoid fine-tuning, we would like $m_h^2 \approx m_{SUSY}^2 \implies m_{SUSY} \leq 1$ TeV. More specifically, knowing $m_H \approx 125$ GeV we expect light SUSY partners (in particular, light stops) near < 1 TeV to stabilize the quadratic divergences of 1 loop corrections to the Higgs mass [citation:*light_stops*]. Unfortunately these scalar partners have yet to be discovered.

It is important to note that the stability of the Higgs boson mass is not the only fine-tuning problem in particle physics. When the same argument is made for the cosmological constant we arrive at $\Lambda \geq m_{SUSY}^4$, where experimentally $\Lambda = 10^{-59}$ TeV⁴. If we use the same SUSY scale as we did for the Higgs mass, $m_{SUSY} = 1$ TeV we have a new fine tuning problem of 10^{60} .

As addressed by Arkani-Hamed and Dimopoulos [citation:*nima_lc*], many theoretical approaches have been motivated by a natural explanation for the Higgs mass while separately seeking an explanation of the cosmological constant through some other mechanism. Arkani-Hamed and Dimopoulos propose a reconsideration of naturalness, entertaining the idea that fine tuning could have a role to play in beyond the

Standard Model physics. Conceivably, both Λ and m_h fine tuning could be resolved by the same mechanism. This un-natural model was further investigated by Giudice and Romanino [citation:*split_{susy}*] and dubbed “split supersymmetry”.

Split SUSY assumes a much higher SUSY scale $m_{SUSY}^2 \gg 1$ TeV where all scalars (excluding the Higgs) become very heavy $O(m_{SUSY})$ and the lightest sparticles (Higgsinos and gluinos) are kept at the TeV scale by requiring the lightest neutralino to be a good dark matter candidate.

Because the scalars are so much heavier, the decay of gluinos through squarks is suppressed. The characteristic signature of split supersymmetry is thus long-lived gluinos; such processes with long lifetimes are rare in the SM.

Chapter 4

Strategies for Discovering New Physics at the LHC

Chapter 5

Displaced Jet Analysis

5.1 Introduction

The study of physics beyond the standard model (BSM) is one of the main objectives of the ATLAS and CMS experiments at the CERN LHC. With no signal observed so far, the ATLAS and CMS results put severe bounds on BSM theories.

The majority of these searches focus on prompt particles with lifetimes $c\tau_0 < 1\text{mm}$ and contain requirements on the physics objects that reject longer lived particle decays. This leaves open the possibility that light long-lived particles could exist and still remain undetected. In this paper, we present an inclusive search for long-lived particles decaying to various combinations of jets and leptons. The analysis exploits the information originating from the CMS calorimeters to reconstruct jets and measure their energies. The information from reconstructed tracks, in particular the transverse impact parameters, is used to discriminate the displaced-jets signal from the background of ordinary multijet events. The analysis is performed on data collected with the CMS detector at a center-of-mass energy $\sqrt{s} = 13 \text{ TeV}$ in 2015. The data set corresponds to an integrated luminosity of 2.7fb^{-1} . Results for similar

signatures have been reported by ATLAS [2, 3] and CMS [4], using data collected at $\sqrt{s} = 8$ TeV.

5.2 Datasets

5.3 Coordinate Conventions

Pseudorapidity η As the detector has cylindrical symmetry, the coordinate system used most commonly is two dimensional (η, ϕ) . The pseudo-rapidity, η is an approximation to rapidity, y , that is exact in the $\beta = 1$ limit:

$$y = \frac{1}{2} \log \frac{E - p_z}{E + p_z} \quad \eta = -\log \left(\tan \left(\frac{\theta}{2} \right) \right)$$

where θ is the angle from the positive beam axis. This variable is useful for a number of reasons. Firstly, differences in rapidity are invariant under longitudinal lorentz boosts along the beam axis. Also, for the energies being probed the particles in the decay products are of negligible mass and the approximation $\eta \approx y$ is nearly exact. Given this relation, pseudorapidity provides an intuitive geometric interpretation. Near full solid angle coverage is provided within $|\eta| < 5$

ΔR Given our coordinate system, ΔR is our longitudinally boost invariant notion of distance:

$$\Delta R = \sqrt{(\Delta\phi)^2 + (\Delta\eta)^2}$$

Fixed values of ΔR form a solid angle “cone” extending from the interaction point outward. This can be seen by using our definition of η to convert from cylindrical

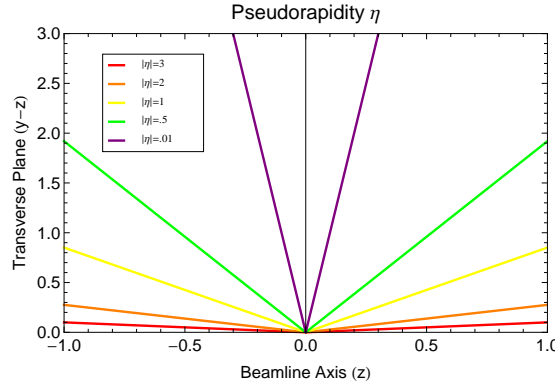


Figure 5.1: Lines of constant pseudorapidity in the z-y plane

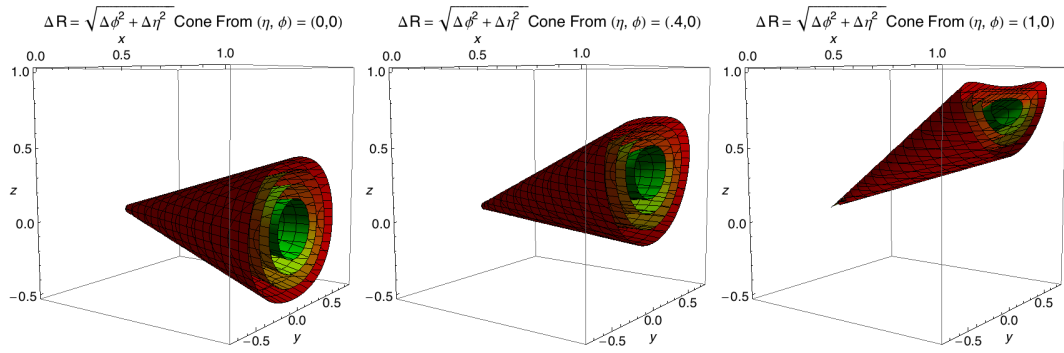


Figure 5.2: Contours of constant ΔR from the $(\eta_0, \phi_0) = 0, 0$

coordinates to (x, y, z) and consider the distance relative to the point (η_0, ϕ_0)

$$\Delta R = \sqrt{(\phi_0 - \tan^{-1}(y/x))^2 + \left(\eta_0 + \log \left(\tan \frac{\cos^{-1}(z/\sqrt{x^2 + y^2})}{2} \right) \right)^2}$$

Table 5.1: Signal efficiency for fixed $m_X = m_{\tilde{t}} = 300$ GeV and varied $c\tau_0$ for the Jet-Jet and B-Lepton models. Selection requirements are cumulative from the first to the last row.

Jet-Jet				
m_X [GeV]	300	300	300	300
$c\tau_0$ [mm]	1	10	100	1000
≥ 2 tags	$2.33 \pm 0.15\%$	$39.49 \pm 0.63\%$	$54.54 \pm 0.74\%$	$14.58 \pm 0.38\%$
Trigger	$2.16 \pm 0.15\%$	$38.12 \pm 0.62\%$	$39.32 \pm 0.63\%$	$8.07 \pm 0.28\%$
Event sel.	$2.09 \pm 0.14\%$	$37.09 \pm 0.61\%$	$36.53 \pm 0.60\%$	$6.67 \pm 0.26\%$
≥ 3 tags	$0.170 \pm 0.041\%$	$14.14 \pm 0.38\%$	$16.72 \pm 0.41\%$	$1.36 \pm 0.12\%$
≥ 4 tags	$0.010 \pm 0.010\%$	$4.73 \pm 0.22\%$	$4.71 \pm 0.22\%$	$0.170 \pm 0.041\%$

B-Lepton				
$m_{\tilde{t}}$ [GeV]	300	300	300	300
$c\tau_0$ [mm]	1	10	100	1000
≥ 2 tags	$0.453 \pm 0.023\%$	$15.82 \pm 0.13\%$	$31.52 \pm 0.19\%$	$8.545 \pm 0.098\%$
Trigger	$0.291 \pm 0.018\%$	$11.45 \pm 0.11\%$	$17.08 \pm 0.14\%$	$3.224 \pm 0.060\%$
Event sel.	$0.269 \pm 0.017\%$	$9.91 \pm 0.11\%$	$13.33 \pm 0.12\%$	$2.084 \pm 0.048\%$
≥ 3 tags	$0.017 \pm 0.004\%$	$2.462 \pm 0.053\%$	$3.814 \pm 0.065\%$	$0.368 \pm 0.020\%$
≥ 4 tags	–	$0.297 \pm 0.018\%$	$0.480 \pm 0.023\%$	$0.0315 \pm 0.0060\%$

5.4 An inclusive displaced-jet tagger

5.5 Event selection

A signal is searched for by applying the selection described in section ?? and counting the number of tagged displaced jets, N_{tags} . In addition to the online and offline requirements described in section 5.6, the analysis signal region requires $N_{\text{tags}} \geq 2$. Efficiencies are reported for all interpreted models as a function of the lifetime with fixed mass (Table 5.1 and 5.2) as well as a function of mass with fixed lifetime (Table 5.3 and 5.4).

The two classes of events: (i) events passing the inclusive trigger algorithm and with $H_T > 650$ GeV; (ii) events passing the exclusive trigger algorithm and with $H_T > 450$ GeV are treated as a single class.

5.6 Datasets and simulated samples

Events are collected from two dedicated online selection algorithms, designed to identify events with displaced jets. The algorithms consider jets clustered from energy deposits in the calorimeters, using the FASTJET [5] implementation of the anti- k_t algorithm [6], with size parameter 0.4. Jets with transverse momentum $p_t < 60$ GeV or $|\eta| > 2.0$ are discarded. An inclusive trigger algorithm accepts events when the scalar sum of the jet p_t 's, H_T , is greater than 500 GeV and at least two jets with $|\eta| < 2.0$ and at most two prompt tracks are found. Tracks are classified as prompt if their transverse impact parameter relative to the beam line, IP^{2D} , is less than 1mm. Another trigger algorithm is used, which requires $H_T > 350$ GeV and asks that there be two displaced jets each having at least one track with transverse impact parameter $IP^{2D} > 5\sigma_{IP^{2D}}$, where $\sigma_{IP^{2D}}$ is the uncertainty on IP^{2D} . Samples with large H_T are used to study the performance of the online selection algorithms.

Events are selected offline requiring at least two jets with $p_t > 60$ GeV and $|\eta| < 2.0$. As for the online selection, the offline jet reconstruction is performed clustering energy deposits in the calorimeters with the anti- k_t algorithm, with jet size parameter of 0.4. Two classes of events are considered: (i) events passing the inclusive trigger algorithm and with $H_T > 650$ GeV and (ii) events passing the exclusive trigger algorithm and with $H_T > 450$ GeV. The two classes of events sum to 786,002 unique events passing the event selection.

The main source of background events originates from multijet production. The properties of this background process are studied using a simulated multijet sample, generated with PYTHIA 8 [7]. The NNPDF 2.3 [8] parton distribution functions (PDFs) are used to model the parton momentum distribution inside the colliding protons. The event simulation includes the effect of multiple proton-proton collisions in the same bunch crossing and in bunch crossing nearby in time, referred to as pileup. Simulated samples are reweighted to match the pileup profile observed in data.

The analysis is interpreted with a set of benchmark signal models. The **Jet-Jet** model predicts pair-produced long-lived scalar neutral particles X^0 [9], each decaying to two light quarks u,d,s,c, and b with equal probability. The resonance mass m_X and proper lifetime $c\tau_0$ are scanned between 50 and 1500 GeV and between 1 and 2000mm, respectively. The trigger efficiencies for a fixed $m_X = 300$ GeV and $c\tau_0 = 1, 30$, and 1000 mm are 30%, 81%, and 42% respectively. The trigger efficiencies for a fixed $c\tau_0 = 30$ mm and $m_X = 50, 100$, and 1000 GeV are 2%, 14%, and 92% respectively.

The **B-Lepton** model contains pair-produced long-lived top squarks in R-parity violating models of Supersymmetry [10]. Each top squark decays to one b quark and a lepton. The branching fractions of the decay to the three lepton flavors are equal. The resonance mass $m_{\tilde{t}}$ and proper lifetime $c\tau_0$ are scanned between 300 and 1000GeV and between 1 and 1000mm, respectively. The trigger efficiencies for a fixed mass $m_{\tilde{t}} = 300$ GeV and $c\tau_0 = 1, 30$, and 1000 mm are 15%, 41%, and 23% respectively. The trigger efficiencies for $m_{\tilde{t}} = 500, 700$, and 1000 GeV and fixed $c\tau_0 = 30$ mm are 64%, 71%, and 74% respectively.

These models are also investigated with modified branching fractions. The **Light-Light** model is the Jet-Jet model excluding decays to b quarks (equal decays to lighter quarks) and the **B-Mu**, **B-Ele**, and **B-Tau** models are derived from the B-Lepton model with 100% branching fraction to muons, electrons, and taus, respectively. Leptonic tau decays are included in the **B-Tau** interpretation. All signal samples are generated with PYTHIA, with the setup described above for the multijet sample.

5.7 Background prediction

As typical multijets contain only a sub dominant fraction of real displaced tracks, jets with a small multiplicity of tracks represent the dominant background. As the

tagging criteria utilize averages of all tracks matched to the jet, the likelihood of tagging a fake decreases exponentially with N_{tracks} .

Figure 5.3 shows the fraction of jets that are tagged as displaced jets in data as a function of the number of tracks associated with the jet N_{tracks} . This function is the misidentification rate of tagging a prompt jet as displaced (up to possible signal contamination) and is interpreted as the probability $p(N_{\text{tracks}})$ of being tagged. This parameterization allows for a representative estimation, event by event, of the probability of tagging multiple fake displaced jets. That is to say, an event with two high track multiplicity jets is much less probable than two single track jets to have 2 fake displaced-jet tags.

To maintain the statistical independence of the events that are used to perform the prediction and the events in the signal region, the probabilities are measured in the full control sample of events with $N_{\text{tags}} \leq 1$, while the final signal region requires $N_{\text{tags}} \geq 2$. Additionally, this limits signal contamination in the probability measurement. The control sample of $N_{\text{tags}} = 1$ includes 1391 events.

The size of the bias introduced by only measuring the misidentification rate in events with $N_{\text{tags}} \leq 1$ is quantifiable. For the nominal tag the size of the effect of removing these events on the predicted number of two tag events is negligible (0.4%) compared to the statistical uncertainty of the prediction.

The mistagging rate is used to predict the probability for an event to have N_{tags} tagged jets, $P(N_{\text{tags}})$. For instance, for an event m with three jets j_1 , j_2 , and j_3 , there is one configuration with no tags, with a probability:

$$P^m(N_{\text{tags}} = 0) = (1 - p_1)(1 - p_2)(1 - p_3) ,$$

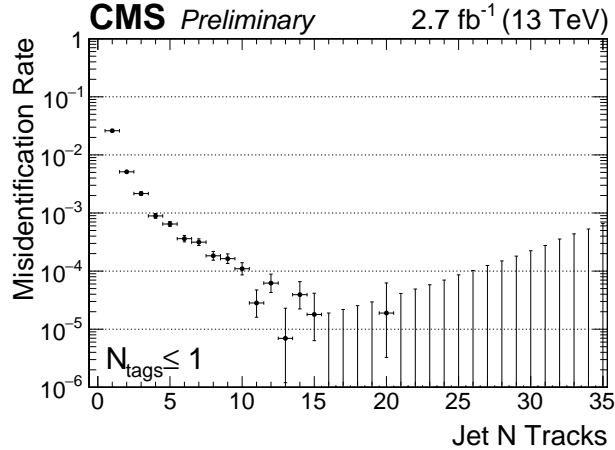


Figure 5.3: The fraction of jets passing the displaced-jet tagging criteria as a function of the number tracks associated with the jet N_{tracks} . The results are from data events with $N_{\text{tags}} \leq 1$ collected with the displaced-jet triggers and passing the offline selection criteria.

where $p_i = p(N_{\text{tracks}}(j_i))$. Similarly, there are three possibilities for this same event to have $N_{\text{tags}} = 1$:

$$P^m(N_{\text{tags}} = 1) = p_1(1 - p_2)(1 - p_3) + (1 - p_1)p_2(1 - p_3) + (1 - p_1)(1 - p_2)p_3 .$$

The probability of finding N_{tags} tags in the m event is:

$$P^m(N_{\text{tags}}) = \sum_{\text{jet-configs}} \prod_{i \in \text{tagged}} p_i \prod_{k \in \text{not-tagged}} (1 - p_k) . \quad (5.1)$$

Tagged jets enter the product as p_i and non-tagged jets enter as $(1 - p_i)$. Equation (5.1) is used to compute the probability of observing N_{tags} , under the assumption that the sample does not contain any signal. The number of events expected for a given value of N_{tags} is then computed as

$$N_{\text{events}}(N_{\text{tags}}) = \sum_m P^m(N_{\text{tags}}) , \quad (5.2)$$

where m runs only over events with fewer than two tagged jets. The prediction is then compared to the observed N_{tags} multiplicity in events with two or more tagged jets, to assess the presence of a signal.

We validate this procedure in the absence (background-only test) and presence (signal-injection test) of a signal, using simulated events.

The background-only test is performed predicting the tag multiplicity on the simulated multijet sample, taking as input the misidentification rate distribution. In order to populate the large- N_{tags} region of the distribution, a looser version of the displaced-jet tagger is employed in this test. The full sample of events passing the event selection is divided into multiple independent samples and the background prediction validated. The predicted background of N_{tags} events in simulated multijet events is found to be consistent within statistical uncertainty.

5.7.1 Signal Injection Tests

Injection with QCD

To test the response of the background prediction to the presence of signal contamination in the jet probabilities used for the $P(N_{\text{tags}})$ derivation, signal events are ‘injected’ into QCD Monte Carlo. Approximately 15 million QCD events from /QCD_HT700to1000_TuneCUETP8M1_13TeV-madgraphMLM-pythia8 are used as the background input. The resulting predictions for varied masses, lifetimes, and sizes of contamination are shown in Fig. 5.4 and Fig. 5.5. The corresponding predictions, observed number of tags, and the deviation from expectation are summarized in Table 5.5 and Table 5.6. The goal of this exercise is to understand the quantity of signal contamination, as well as lifetime and mass, required to significantly alter the background prediction.

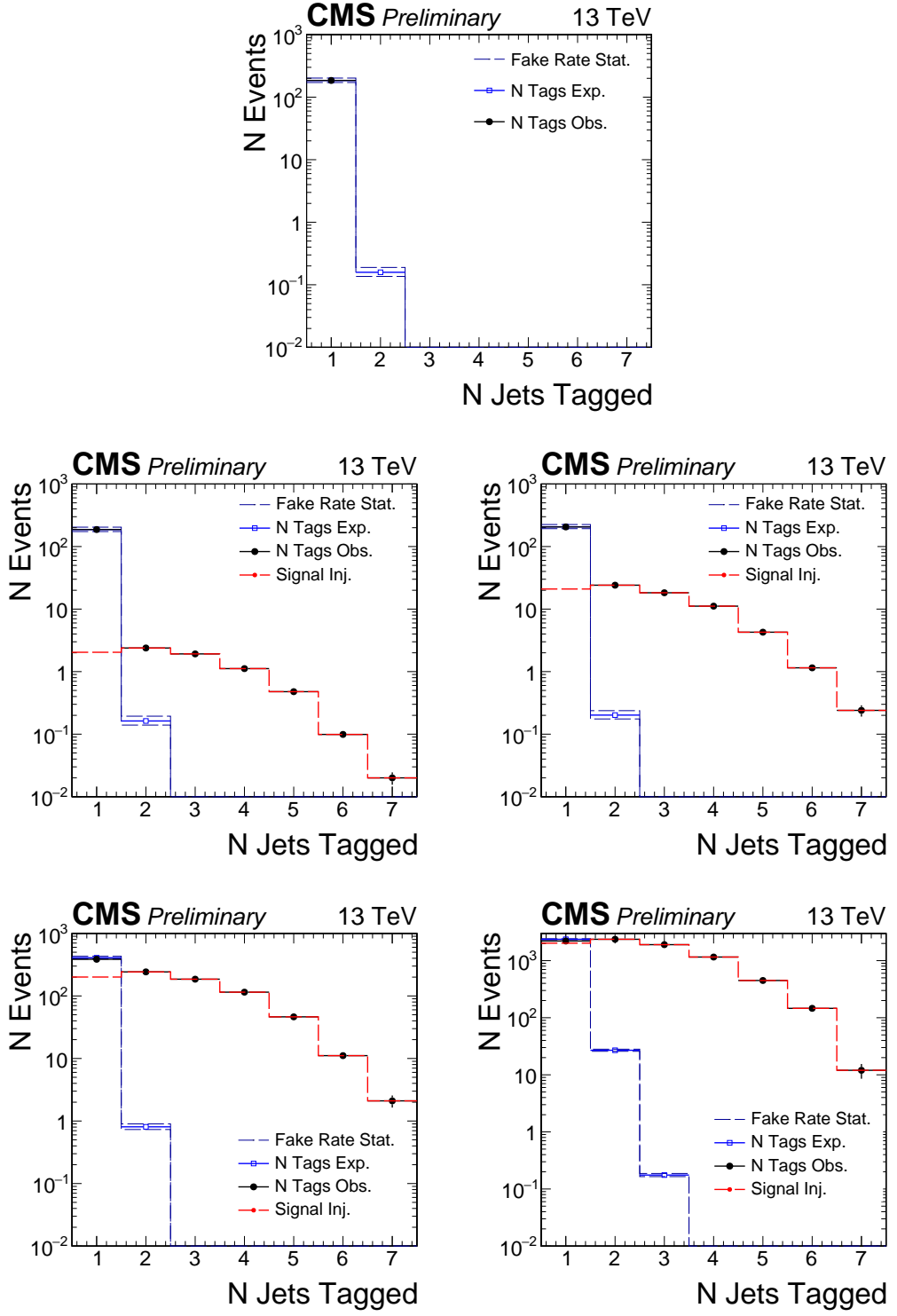


Figure 5.4: Signal Injection tests. The Jet-Jet signal sample used has fixed $m_X = 700\text{GeV}$ and $c\tau_0 = 10 \text{ mm}$. The level of signal contamination is progressively varied between 10, 100, 1000, and 10000 events injected before any selection. The full event selection is applied and the baseline jet tag definition.

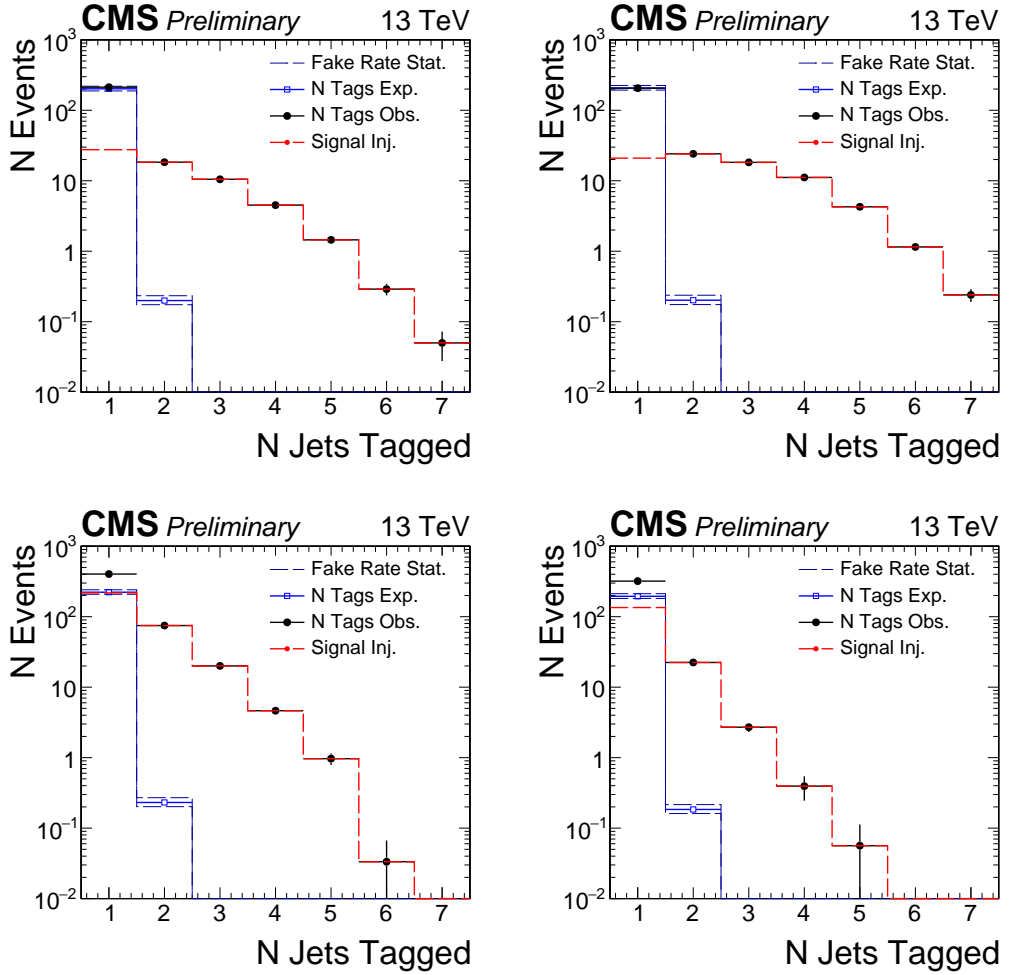


Figure 5.5: Signal Injection. The Jet-Jet signal sample is varied $m_X = 700 \text{ GeV}$ and $c\tau_0 = 1000 \text{ mm}$ (top left) $m_X = 700 \text{ GeV}$ and $c\tau_0 = 10 \text{ mm}$ (top right) $m_X = 100 \text{ GeV}$ and $c\tau_0 = 1000 \text{ mm}$ (bottom left) $m_X = 100 \text{ GeV}$ and $c\tau_0 = 10 \text{ mm}$ (bottom right). The level of signal contamination is fixed at 100 events for the $m_X = 700 \text{ GeV}$ and 1000 events for $m_X = 100 \text{ GeV}$. The full event selection is applied and the baseline jet tag definition.

The resulting predictions are also reported normalized such that the total signal + qcd events passing the event selection are equal to the number of events passing the event selection in the analysis in Table 5.7.

The change in the N_{tags}^{obs} distribution to the presence of signal is on the order of the number of events with $N_{tags} > 2$ whereas the integrated shift in $P(N_{tags} \geq 2)$ is on the order of the shift induced in the $p(j)$ distribution. This shift is of the order the signal contamination. We can conclude the analysis will retain relative sensitivity as long as the signal contamination is relatively smaller than the QCD contribution in the fake rate calculation.

In summary, the background prediction is robust to a variety signal masses, lifetimes and sizes of contamination. Robust in the sense that the background is correctly determined within error in the 0 injection case and the bias to the background prediction due to the contamination is small relative to the number of signal events injected.

The following section explores the sensitivity to signal explicitly in a simplified scenario given the assumption that the jet probabilities accurately predict the background in the scenario where there are no signal events present. This assumption is based on the closure studies in the previous section and be considered true within some closure systematic.

Explicit Sensitivity in A Simplified Injection Scenario

Consider a sample of N_{QCD} QCD events with a known fraction of jets that are tagged $f(j_i)$ as a function of some jet parameters j_i . For simplicity, assume events have exactly 2 jets. Also assume we have shown that the observation approximately determined $N_{obs}^{2tag} = N_{pred}^{2tag}$ when we interpret $f(j_i)$ as a conditional probability $p(j_i)$ such

that:

$$N_{obs}^{2tag} = N_{pred}^{2tag} = \sum_i [p(j_1)p(j_2)]_i = N_{QCD} p^2$$

where we are using a flat probability p such that $p(j_1) = p(j_2) = p = n_{tag}/n_{jets} = n_{fake}/2N_{events}$. Where n_{tag} is the number of jets tagged, which in a QCD sample is exactly n_{fake} . Now, say we perform the signal injection test by injecting N_{sig} events with correspondingly $2N_{sig}$ signal jets. Let ϵ be the efficiency for a signal event to have 1 tag. Accordingly the probability will shift $p(j_i) \rightarrow \tilde{p}(j_i)$:

$$\tilde{p} = \frac{n_{fake} + n_{true-tags}}{2N_{QCD} + 2N_{sig}} = \frac{n_{fake} + \epsilon 2N_{sig}}{2N_{QCD} + 2N_{sig}}$$

Taylor expanding in N_{sig} about 0 we obtain:

$$\begin{aligned} \tilde{p} &= \frac{n_{fake}}{2N_{QCD}} - \frac{N_{sig}n_{fake}}{2(N_{QCD})^2} + \epsilon \frac{2N_{sig}N_{QCD}}{2(N_{QCD})^2} \\ &= p - p \frac{N_{sig}}{N_{QCD}} + \frac{N_{sig}\epsilon}{N_{QCD}} \end{aligned}$$

Let $\Delta = N_{sig}/N_{QCD}$

$$\tilde{p} = p(1 - \Delta) + \Delta\epsilon$$

Note that as the signal contamination $\Delta \rightarrow 0$, we obtain the correct probability $\tilde{p} = p$.

Now we attempt to predict the number of events with 2 tags using \tilde{p} and splitting

the sum over signal and QCD events.

$$\begin{aligned}
N_{pred}^{2tag} &= \sum_i \tilde{p}\tilde{p} \\
&= \sum_i (p(1 - \Delta) + \Delta\epsilon)^2 \\
&= \sum_i p^2 - p^2(2\Delta) + p^2\Delta^2 + 2p\Delta\epsilon - 2p\Delta^2\epsilon + \Delta^2\epsilon^2
\end{aligned}$$

We now split the events in the sum between QCD and Signal.

$$\begin{aligned}
N_{pred}^{2tag} &= \sum_i (QCD) + \sum_i (Signal) \\
\sum_i (QCD) &= N_{QCD}(p^2 - p^2(2\Delta) + p^2\Delta^2 + 2p\Delta\epsilon - 2p\Delta^2\epsilon + \Delta^2\epsilon^2) \\
&= N_{obs}^{QCD} - N_{sig}(p^2\Delta + \Delta\epsilon^2 - 2p^2 + 2p\epsilon - 2p\Delta\epsilon)
\end{aligned}$$

where we have used the fact that $\Delta N_{QCD} = N_{sig}$ and $\sum_i p^2 = N_{obs}^{QCD}$:

$$\sum_i (Signal) = N_{sig}(p^2 - p^2(2\Delta) + p^2\Delta^2 + 2p\Delta\epsilon - 2p\Delta^2\epsilon + \Delta^2\epsilon^2)$$

We now evaluate our sensitivity to signal or equivalently the disagreement between observed and prediction by the variable S . Let $N_{obs}^{2tag} = N_{obs}^{sig} + N_{obs}^{QCD}$. The sensitivity S , is a measure of how well we have predicted the background in the presence of signal. When $S = 1$ the prediction is exactly the background and the excess is exactly the number of signal events. When $S = 0$ the probabilities prediction has over estimated the background entirely resulting in no disagreement between observed and predicted

2 tag events.

$$\begin{aligned}
S = \frac{N_{obs}^{2tag} - N_{pred}^{2tag}}{N_{sig}} &= 1 - (2p\epsilon + \Delta\epsilon^2) \\
&\quad - (p^2 + \Delta^2\epsilon^2 + 2p\Delta\epsilon - 2p^2 - 2p\Delta\epsilon) \\
&\quad - (p^2\Delta - 2p^2\Delta - 2p\Delta^2\epsilon) \\
&\quad - (p^2\Delta^2)
\end{aligned}$$

where we have grouped terms by their order in $O(\Delta) + O(p)$. Consider the case when $\epsilon \approx 1$ (this is an approximation for readability as $\epsilon = 1$ would imply no 2 tag events) and for simplicity say $\Delta = p = x$.

$$S = 1 - 3x + 3x^3 - x^4$$

If we plug in the baseline fake rate for x then $S(x = 5 \times 10^{-4}) = 0.999$.

5.7.2 Tag Probability Cross Validation

To test the bias of the background estimation a method of cross validation is utilized. For a given sample, N_{div} non-overlapping sub-samples are partitioned. For each sub-sample, a corresponding set of jet probabilities are computed as described in the previous section. For each set of jet probabilities, an N_{tag}^{pred} prediction is made for the $N_{div} - 1$ remaining samples (which have no overlapping events). We will refer to the sample used for the prediction as the measurement sample. The result is $N_{div}(N_{div} - 1)$ pairs of probabilities and measurement samples. From each pair, in each bin of N_{tags} , we generate a distribution of pulls $(N_{obs} - N_{pred})/\sqrt{N_{pred}}$ for each N_{tag} bin. All events must pass the event selection.

Due to limited statistics in the 2 tag bin for the baseline tag, the loose tag definition (Table ??) is used to generate pull distributions in the 2 tag bin.

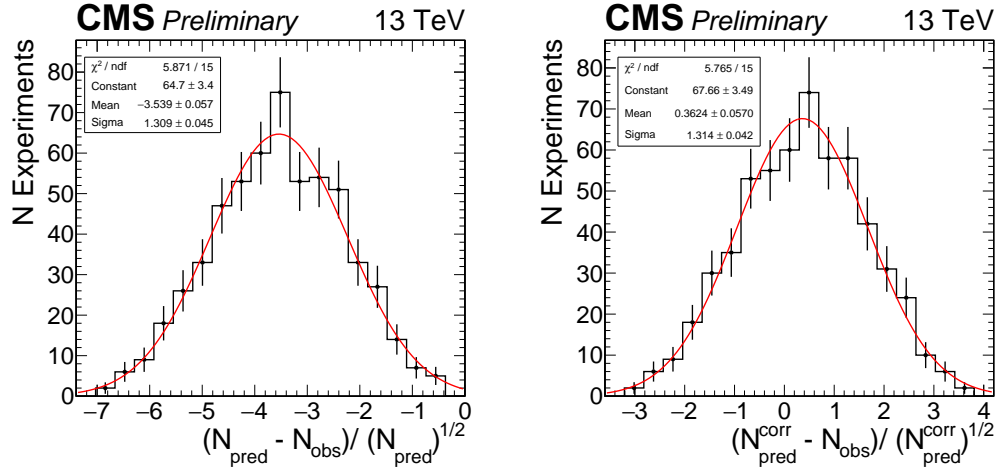


Figure 5.6: Cross validation of the predicted of the number of loose tags in data collected by the displaced jet triggers. Pulls for the 1 tag bin with the loose tag (left). Pulls for the 1 tag bin with the loose tag with the SR correction (Right).

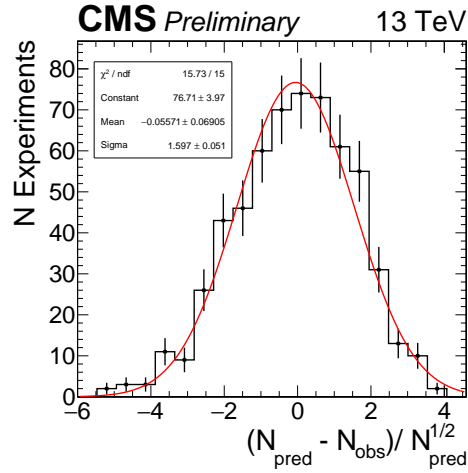


Figure 5.7: Cross validation of the predicted of the number of tags in data passing the displaced jet triggers. Pulls for the 1 tag bin with the baseline tag after the application of the signal removal correction $2r_{12} = .2\%$

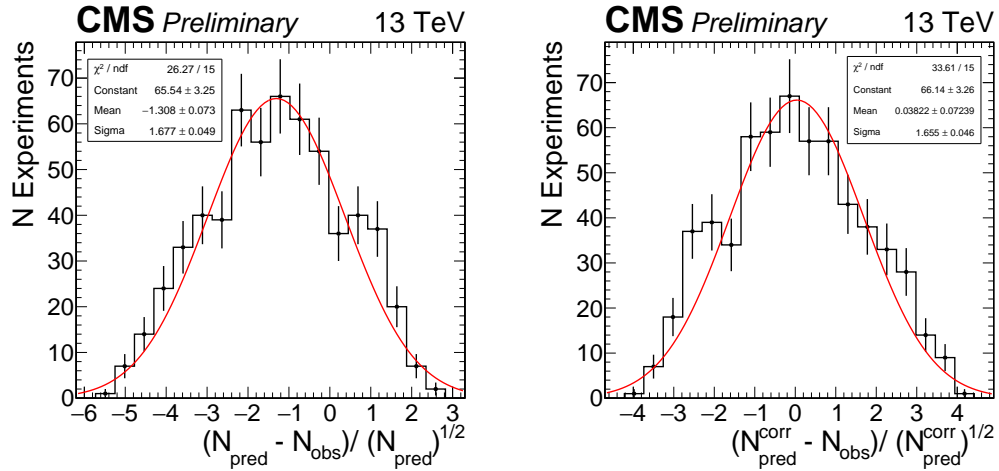


Figure 5.8: Cross validation of the predicted of the number of loose tags in QCD events passing the displaced jet triggers. Pulls for the 1 tag bin with the loose tag (left). The signal region removal corrected pulls (Right).

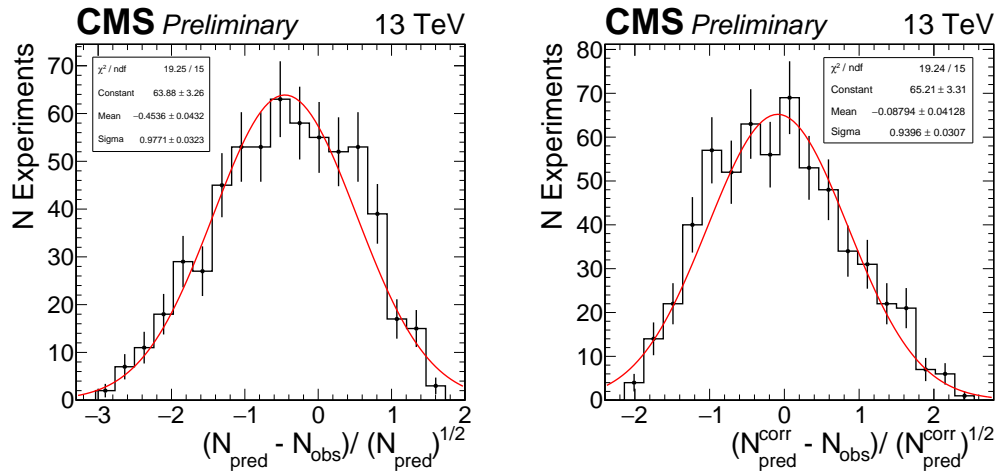


Figure 5.9: Cross validation of the predicted of the number of loose tag in QCD events passing the displaced jet triggers. Pulls for the 2 tag bin with the loose tag uncorrected (left). The same prediction corrected for the SR removal (right)

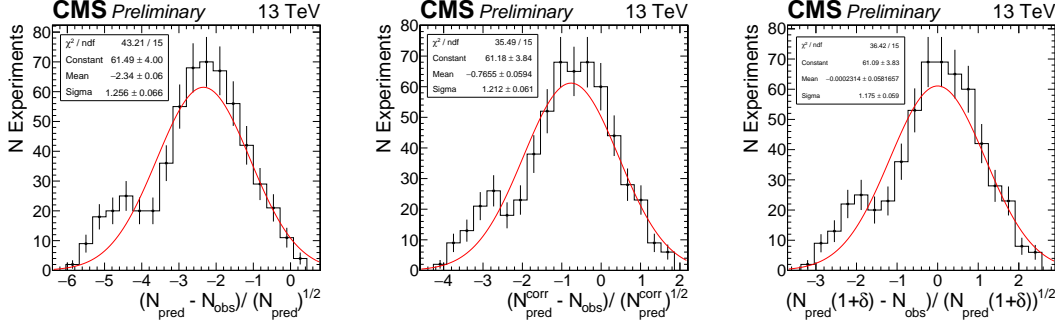


Figure 5.10: Cross validation of the predicted of the number of baseline tags in data collected by the displaced jet triggers. Pulls for the 2 tag bin with the loose tag (left). Pulls with the signal region removal correction applied (middle). The same signal region removal correction shifted by $\delta = 7.5\%$ (Right).

We summarize the cross validation studies in the following figures:

- Fig 5.6: SR corrected and uncorrected 1 tag bin pulls for the Loose tag definition in Data collected by Displaced Jet Triggers. $N_{div} = 25$
- Fig 5.7: SR corrected 1 tag bin pulls for the Baseline tag definition in Data collected by Displaced Jet Triggers. $N_{div} = 25$
- Fig 5.8: 1 tag bin pulls for the Loose tag definition in QCD events passing the Displaced Jet Triggers. $N_{div} = 25$
- Fig 5.9: 2 tag bin pulls for the Loose tag definition in QCD events passing by Displaced Jet Triggers. $N_{div} = 25$
- Fig 5.10: SR corrected, uncorrected, and SR corrected+ δ 2 tag bin pulls for the Loose tag definition in Data collected by Displaced Jet Triggers. $N_{div} = 25$

In data and QCD, the SR correction provides a significant improvement on the pull distributions with respect to the ideal parameters $\mu = 0$ and $\sigma = 1.0$. For the 1 tag prediction in data with the loose tag the central value changes from $\mu = 3.5$ (uncorrected) to $\mu = 0.36$ (corrected). For the signal region (2+ tags), the loose tag

in data is within 7.5% of ideal μ and the QCD estimate is within error of $\mu = 0$ but has $\sigma = 1.6 > 1.0$.

5.8 Systematic uncertainties

5.8.1 Background systematic uncertainties

A background systematic uncertainty is quoted for the data-driven background prediction method. This uncertainty is estimated by repeating the background-prediction procedure on data with a looser version of the displaced-jet tagging algorithm as outlined in section 5.7. The background estimation uncertainty of 7.5% is the required adjustment to the prediction to remove the bias observed in the Gaussian fit. For three or more tags, the systematic uncertainty for the method is kept fixed.

The statistical uncertainty on the measured misidentification rate as a function of N_{tracks} is propagated to the predicted N_{tags} distribution as a systematic uncertainty. This systematic uncertainty is calculated for each tag multiplicity bin individually. The uncertainty for the 2 tag bin is $-12/+13\%$.

In summary, for the background prediction in the two tag bin, a 7.5% uncertainty is assigned to the background prediction method and $-12/+13\%$ uncertainty is assigned to the statistics of the misidentification rate.

5.8.2 Signal systematic uncertainties

A summary of the systematic uncertainties associated with the signal yields is given in Table 5.8. The uncertainty on the trigger emulation is measured by comparing the predicted efficiency for simulated multijet events and data collected by a loose H_T trigger. The observed difference at threshold (5%) is taken as an estimate of the uncertainty in the emulation of the online H_T requirement. Similarly, the uncertainty induced by the online versus offline jet acceptance is obtained from the shift in the

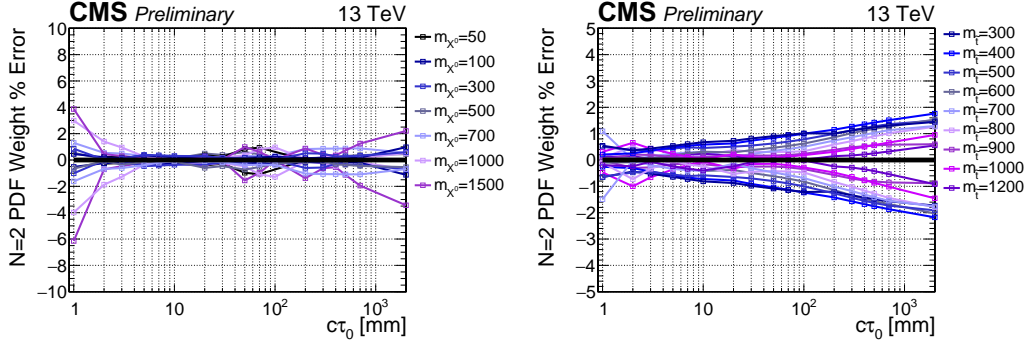


Figure 5.11: The PDF acceptance systematics in the Jet-Jet (left) and B-Lepton (right) signal model as a function of the mass m_X or $c\tau_0$ for the 2 tag bin. The systematic is reported two sided for the two tag bin in the analysis. The error to fluctuate up is in the upper half plane and the error to fluctuate down on the lower half plane.

trigger efficiency when the offline jet p_t requirement is increased from $p_t > 60$ GeV to $p_t > 80$ GeV (5%).

The systematic uncertainty on the luminosity is 2.7% [11].

The uncertainty arising from the PDFs for pair-produced masses in the range of 50–1500 GeV is found to be 1–6% Figure 5.11. An ensemble of alternative PDF is sampled from the output of the NNPDF fit. Events are reweighted according to the ratio between these alternative PDF sets and the nominal ones. The distribution of the signal prediction for these PDF ensemble is used to quantify the uncertainty.

The systematic uncertainty on the modeling of the jet tagging variables in signal MC samples is estimated from the displaced track modeling in multi-jet events in data and MC. The mismodeling of the measured value of Θ_{2D} and IP_{sig}^{2D} for single tracks is propagated to the final tag distribution by varying the individual measured values in MC by the difference in the measured value relative to data (3–10%). The tagging variables are then re-calculated. The N_{tags} distribution is recalculated with the new values. The systematic uncertainty is assigned as the relative change in events, bin by bin in N_{tags} . For the two tag bin, this varies from 1 to 30% depending on the mass

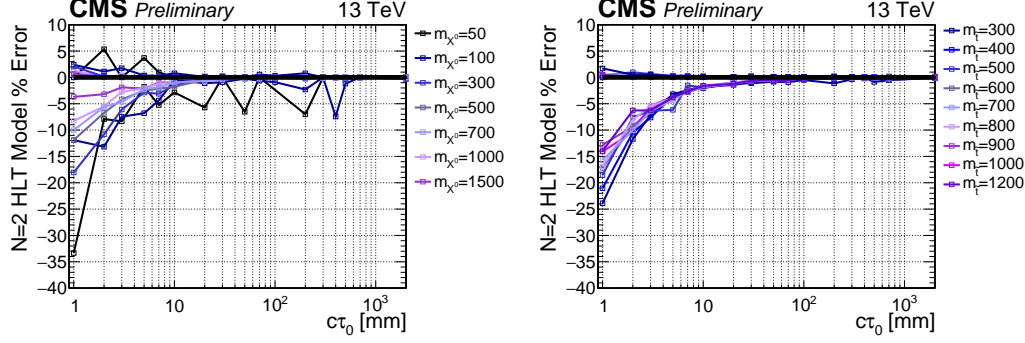


Figure 5.12: The onling tracking related systematics in the Jet-jet (left) and B-Lepton (right) model as a function of $c\tau_0$. (Top) The online track 2DIP and 2DIP_{*sig*} modeling in the 2 tag bin

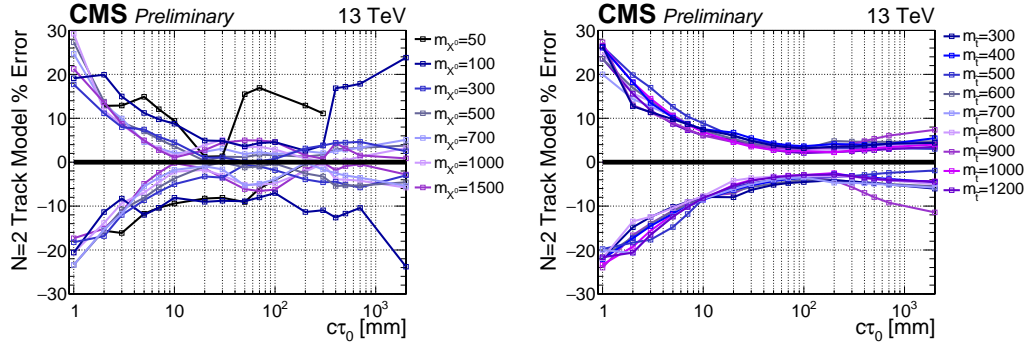


Figure 5.13: The two tracking related systematics in the Jet-Jet (left) and B-Lepton (right) model as a function of $c\tau_0$. The displaced jet tagging variable systematic in the 2 tag bin. The systematic is reported two sided for the two tag bin in the analysis. The error to fluctuate up is in the upper half plane and the error to fluctuate down on the lower half plane.

and lifetime Figure 5.13. The mismodeling of α_{\max} is found to have a negligible effect on the signal efficiency as the requirement is relatively loose.

The systematic uncertainty on the modeling of the online tracking efficiency is obtained by studying the online regional track reconstruction in data and MC. The online values of IP^{2D} and IP_{sig}^{2D} are varied by the magnitude of the mismodeling found in events collected in control triggers. The new values are used to determine if the event would still pass at least one of the trigger paths and its associated offline H_T requirement. The N_{tags} distribution is recalculated with the values varied up and down. The relative change in the number of events per bin is taken as the systematic uncertainty. For the two tag bin, this uncertainty varies from 1 to 35%.

All signal systematic uncertainties are calculated individually for each model for all individual mass and lifetime points, and for each value of N_{tags} in the signal region.

5.9 Results and interpretation

The numerical values for the expected and observed yields are summarized in Table 5.9. The observed yields are found to be consistent with the predicted background, within the statistical and systematic uncertainties. No evidence for a signal at large values of N_{tags} is observed.

Exclusions for each model are obtained from the predicted and observed event yields in Table 5.9 and the signal efficiencies in Tables 5.3–5.4. All bounds are derived at 95% confidence-level (CL) according to the CL_s prescription [12, 13, 14] in the asymptotic approximation. For each limit derivation, we consider events with $N_{\text{tags}} \geq 2$ using independent bins for $N_{\text{tags}} = 2$ and $N_{\text{tags}} \geq 3$. Finer binning of the tag multiplicity for $N_{\text{tags}} > 3$ is found to have a negligible affect on the expected limits. Cross section upper limits are presented as a function of the mass and lifetime of the parent particle. The analysis sensitivity is maximal for $(10 < c\tau_0 < 1000)\text{mm}$.

Mass exclusion bounds at fixed lifetime are also derived, comparing the excluded cross section with the values predicted for the benchmark models described in section 5.6. In the case of SUSY models, the next-to-leading order (NLO) and next-to-leading-logs (NLL) $t\tilde{t}$ production cross section is used as reference, computed in the large-mass limit for all the other SUSY particles [15, 16, 17, 18, 19, 20].

Figures 5.14 and 5.15 show the excluded pair-production cross section for the Jet-Jet and Light-Light models, respectively. Cross sections as small as 1.2 fb are excluded for $c\tau_0 = 50\text{mm}$ for both models. Exclusion limits are also derived for resonances decaying to $b\ell$ final states, as shown in Fig. 5.16. The sensitivity is similar to what is observed for the Jet-Jet model, although less stringent as additional jets give higher efficiency than additional leptons from both the tagging and triggering perspectives. Cross sections larger than 2.47 fb are excluded at 95% CL, for $c\tau_0$ in the range 70–100 mm excluding a parent mass value of 1135 GeV.

Figures 5.17 and 5.18 show the exclusions on the B-Tau and B-Ele models, respectively. The two models have similar performance at high mass with slightly stronger limits for the B-Ele model at lower mass $m_{\tilde{t}} = 300\text{ GeV}$ and lifetimes $c\tau_0 > 10\text{mm}$. The highest mass excluded in the B-Ele (B-Tau) model occurs at $m_{\tilde{t}} = 1150$ (1155)GeV and $c\tau_0 = 70$ (70)mm at an observed cross section upper limit of 2.25 (2.17) fb at 95% CL.

In contrast, Fig. 5.19 shows the exclusion for the B-Mu model. Since the analysis uses jets reconstructed from calorimetric deposits while the two muons have small or no associated calorimeter deposit, the signal reconstruction efficiency and displaced-jet multiplicity are smaller in this case. This results in a weaker exclusion bound. The highest mass excluded in the B-Mu model occurs at $m_{\tilde{t}} = 1090\text{ GeV}$ and $c\tau_0 = 70\text{mm}$ at an observed cross section upper limit of 3.36 fb at 95% CL.

Table 5.2: Signal efficiency for fixed $m_X = m_{\tilde{t}} = 300$ GeV and varied $c\tau_0$ with modified branching ratios relative to the Jet-Jet and B-Lepton models. Selection requirements are cumulative from the first to the last row.

Light-Light				
m_X [GeV]	300	300	300	300
$c\tau_0$ [mm]	1	10	100	1000
≥ 2 tags	$2.20 \pm 0.19\%$	$40.49 \pm 0.80\%$	$54.92 \pm 0.93\%$	$14.55 \pm 0.47\%$
Trigger	$2.04 \pm 0.18\%$	$39.16 \pm 0.78\%$	$39.63 \pm 0.79\%$	$8.20 \pm 0.36\%$
Event sel.	$2.03 \pm 0.18\%$	$38.41 \pm 0.77\%$	$36.99 \pm 0.76\%$	$6.89 \pm 0.33\%$
≥ 3 tags	$0.187 \pm 0.054\%$	$14.77 \pm 0.48\%$	$16.70 \pm 0.51\%$	$1.48 \pm 0.15\%$
≥ 4 tags	–	$5.11 \pm 0.28\%$	$4.73 \pm 0.27\%$	$0.216 \pm 0.058\%$
B-Ele				
$m_{\tilde{t}}$ [GeV]	300	300	300	300
$c\tau_0$ [mm]	1	10	100	1000
≥ 2 tags	$0.807 \pm 0.093\%$	$20.51 \pm 0.47\%$	$39.01 \pm 0.65\%$	$11.46 \pm 0.35\%$
Trigger	$0.398 \pm 0.065\%$	$14.68 \pm 0.40\%$	$22.95 \pm 0.50\%$	$5.15 \pm 0.23\%$
Event sel.	$0.398 \pm 0.065\%$	$13.92 \pm 0.39\%$	$20.34 \pm 0.47\%$	$3.58 \pm 0.19\%$
≥ 3 tags	$0.043 \pm 0.022\%$	$4.22 \pm 0.21\%$	$7.21 \pm 0.28\%$	$0.822 \pm 0.093\%$
≥ 4 tags	–	$0.727 \pm 0.088\%$	$1.19 \pm 0.11\%$	$0.053 \pm 0.024\%$
B-Tau				
$m_{\tilde{t}}$ [GeV]	300	300	300	300
$c\tau_0$ [mm]	1	10	100	1000
≥ 2 tags	$0.483 \pm 0.073\%$	$18.40 \pm 0.45\%$	$34.98 \pm 0.61\%$	$9.31 \pm 0.32\%$
Trigger	$0.439 \pm 0.069\%$	$14.63 \pm 0.40\%$	$20.20 \pm 0.46\%$	$3.81 \pm 0.20\%$
Event sel.	$0.406 \pm 0.067\%$	$12.45 \pm 0.37\%$	$15.50 \pm 0.41\%$	$2.37 \pm 0.16\%$
≥ 3 tags	$0.022 \pm 0.016\%$	$3.23 \pm 0.19\%$	$4.62 \pm 0.22\%$	$0.441 \pm 0.069\%$
≥ 4 tags	–	$0.525 \pm 0.076\%$	$0.660 \pm 0.084\%$	$0.022 \pm 0.015\%$
B-Mu				
$m_{\tilde{t}}$ [GeV]	300	300	300	300
$c\tau_0$ [mm]	1	10	100	1000
≥ 2 tags	$0.130 \pm 0.037\%$	$8.02 \pm 0.29\%$	$20.09 \pm 0.46\%$	$4.03 \pm 0.21\%$
Trigger	$0.054 \pm 0.024\%$	$3.97 \pm 0.21\%$	$6.63 \pm 0.26\%$	$0.881 \pm 0.098\%$
Event sel.	$0.043 \pm 0.022\%$	$2.92 \pm 0.18\%$	$4.21 \pm 0.21\%$	$0.489 \pm 0.073\%$
≥ 3 tags	–	$0.227 \pm 0.049\%$	$0.307 \pm 0.057\%$	$0.033 \pm 0.019\%$
≥ 4 tags	–	$0.011 \pm 0.011\%$	–	–

Table 5.3: Signal efficiencies for the Jet-Jet and B-Lepton models with $c\tau_0 = 30\text{mm}$ and varied mass. Selection requirements are cumulative from the first to the last row.

Jet-Jet				
m_X [GeV]	50	100	300	1000
$c\tau_0$ [mm]	30	30	30	30
≥ 2 tags	$2.710 \pm 0.095\%$	$14.80 \pm 0.22\%$	$54.24 \pm 0.74\%$	$79.93 \pm 0.89\%$
Trigger	$0.503 \pm 0.041\%$	$5.39 \pm 0.13\%$	$46.41 \pm 0.68\%$	$74.05 \pm 0.86\%$
Event sel.	$0.297 \pm 0.031\%$	$3.70 \pm 0.11\%$	$44.75 \pm 0.67\%$	$73.99 \pm 0.86\%$
≥ 3 tags	$0.050 \pm 0.013\%$	$1.087 \pm 0.060\%$	$20.87 \pm 0.46\%$	$49.42 \pm 0.70\%$
≥ 4 tags	–	$0.217 \pm 0.027\%$	$6.81 \pm 0.26\%$	$25.45 \pm 0.50\%$

B-Lepton				
$m_{\tilde{t}}$ [GeV]	300	600	800	1000
$c\tau_0$ [mm]	30	30	30	30
≥ 2 tags	$31.52 \pm 0.19\%$	$47.32 \pm 0.23\%$	$52.53 \pm 0.24\%$	$55.88 \pm 0.35\%$
Trigger	$17.08 \pm 0.14\%$	$35.03 \pm 0.20\%$	$40.40 \pm 0.21\%$	$43.14 \pm 0.30\%$
Event sel.	$14.70 \pm 0.13\%$	$32.34 \pm 0.19\%$	$36.94 \pm 0.20\%$	$39.26 \pm 0.29\%$
≥ 3 tags	$4.106 \pm 0.068\%$	$10.76 \pm 0.11\%$	$13.29 \pm 0.12\%$	$15.00 \pm 0.18\%$
≥ 4 tags	$0.552 \pm 0.025\%$	$1.828 \pm 0.045\%$	$2.687 \pm 0.055\%$	$3.092 \pm 0.082\%$

Table 5.4: Signal efficiency for fixed $c\tau_0 = 30$ mm and varied mass with modified branching ratios relative to the Jet-Jet and B-Lepton models. Selection requirements are cumulative from the first to the last row.

Light-Light					
m_X [GeV]	50	100	300	1000	
$c\tau_0$ [mm]	30	30	30	30	
≥ 2 tags	$2.84 \pm 0.12\%$	$15.56 \pm 0.29\%$	$54.87 \pm 0.92\%$	$80.52 \pm 1.11\%$	
Trigger	$0.530 \pm 0.052\%$	$5.70 \pm 0.17\%$	$47.14 \pm 0.85\%$	$74.85 \pm 1.07\%$	
Event sel.	$0.327 \pm 0.041\%$	$3.90 \pm 0.14\%$	$45.68 \pm 0.84\%$	$74.80 \pm 1.07\%$	
≥ 3 tags	$0.052 \pm 0.016\%$	$1.113 \pm 0.076\%$	$21.77 \pm 0.58\%$	$50.04 \pm 0.88\%$	
≥ 4 tags	–	$0.230 \pm 0.035\%$	$7.38 \pm 0.34\%$	$25.80 \pm 0.63\%$	
B-Ele					
$m_{\tilde{t}}$ [GeV]	300	600	800	1000	
$c\tau_0$ [mm]	30	30	30	30	
≥ 2 tags	$39.01 \pm 0.65\%$	$53.70 \pm 0.75\%$	$59.62 \pm 0.78\%$	$62.42 \pm 1.11\%$	
Trigger	$22.95 \pm 0.50\%$	$38.07 \pm 0.63\%$	$43.06 \pm 0.66\%$	$45.21 \pm 0.95\%$	
Event sel.	$21.59 \pm 0.48\%$	$37.02 \pm 0.62\%$	$39.47 \pm 0.64\%$	$42.20 \pm 0.92\%$	
≥ 3 tags	$7.86 \pm 0.29\%$	$14.28 \pm 0.38\%$	$17.37 \pm 0.42\%$	$20.39 \pm 0.64\%$	
≥ 4 tags	$1.37 \pm 0.12\%$	$3.32 \pm 0.19\%$	$4.34 \pm 0.21\%$	$4.69 \pm 0.31\%$	
B-Tau					
$m_{\tilde{t}}$ [GeV]	300	600	800	1000	
$c\tau_0$ [mm]	30	30	30	30	
≥ 2 tags	$34.98 \pm 0.61\%$	$51.42 \pm 0.73\%$	$57.20 \pm 0.76\%$	$59.43 \pm 1.07\%$	
Trigger	$20.20 \pm 0.46\%$	$39.78 \pm 0.64\%$	$45.46 \pm 0.68\%$	$47.62 \pm 0.96\%$	
Event sel.	$17.17 \pm 0.43\%$	$37.47 \pm 0.62\%$	$43.64 \pm 0.67\%$	$44.26 \pm 0.92\%$	
≥ 3 tags	$5.21 \pm 0.24\%$	$13.29 \pm 0.37\%$	$16.15 \pm 0.40\%$	$19.13 \pm 0.61\%$	
≥ 4 tags	$0.86 \pm 0.10\%$	$3.09 \pm 0.18\%$	$3.68 \pm 0.19\%$	$4.48 \pm 0.29\%$	
B-Mu					
$m_{\tilde{t}}$ [GeV]	300	600	800	1000	
$c\tau_0$ [mm]	30	30	30	30	
≥ 2 tags	$20.09 \pm 0.46\%$	$35.46 \pm 0.60\%$	$41.18 \pm 0.64\%$	$43.13 \pm 0.93\%$	
Trigger	$6.63 \pm 0.26\%$	$24.73 \pm 0.50\%$	$31.85 \pm 0.56\%$	$34.10 \pm 0.82\%$	
Event sel.	$5.25 \pm 0.24\%$	$21.40 \pm 0.47\%$	$27.42 \pm 0.52\%$	$31.18 \pm 0.79\%$	
≥ 3 tags	$0.344 \pm 0.060\%$	$3.03 \pm 0.18\%$	$5.28 \pm 0.23\%$	$6.08 \pm 0.35\%$	
≥ 4 tags	–	$0.122 \pm 0.035\%$	$0.677 \pm 0.082\%$	$0.68 \pm 0.12\%$	

Table 5.5: The signal injection test using a fixed signal point $m_X = 700$ GeV and $c\tau_0 = 10\text{mm}$ with varied amount of injection. A summary of the 1,2,3, and 4 tag predictions as a function of the number of events injected (top). The two background systematic errors are listed separately as $\sigma_{method}, \sigma_{fake-rate}$. A summary of the observed number of tags (bottom).

Injection $\sigma \times \mathcal{L}$	1 Tag Pred	2 Tag Pred	3 Tag Pred	4 Tag Pred
0	$185^{+14,+17}_{-14,-13}$	$0.16^{+0.01,+0.03}_{-0.01,-0.02}$	—	—
10	$187^{+14,+17}_{-14,-13}$	$0.16^{+0.01,+0.03}_{-0.01,-0.02}$	—	—
100	$207^{+16,+18}_{-16,-14}$	$0.20^{+0.02,+0.04}_{-0.02,-0.03}$	—	—
1000	$408^{+31,+23}_{-31,-19}$	$0.81^{+0.06,+0.09}_{-0.06,-0.08}$	—	—
10000	$2366^{+177,+53}_{-177,-49}$	$26.95^{+2.02,+1.19}_{-2.02,-1.10}$	$0.18^{+0.01,+0.01}_{-0.01,-0.01}$	—

Injection $\sigma \times \mathcal{L}$	1 Tag Obs	2 Tag Obs	3 Tag Obs	4 Tag Obs
0	185.00	0.00	0.00	0.00
10	186.94	2.40	1.99	1.20
100	205.14	23.05	20.45	11.89
1000	386.10	237.20	188.40	116.80
10000	2260.00	2341.00	1976.00	1165.00

Table 5.6: Signal injection test with fixed number of injected events and varied $c\tau_0$ and m_X . A summary of the 1,2,3, and 4 tag predictions as a function of the number of events injected (top). The two background systematic errors are listed separately as $\sigma_{method}, \sigma_{fake-rate}$. A summary of the observed number of tags (bottom).

$\sigma \times \mathcal{L}$	Mass [GeV]	$c\tau_0$ [mm]	1 Tag Pred	2 Tag Pred	3 Tag Pred	4 Tag Pred
100	700	10	$207^{+16,+18}_{-16,-14}$	$0.20^{+0.02,+0.04}_{-0.02,-0.03}$	—	—
100	700	1000	$202^{+15,+18}_{-15,-14}$	$0.20^{+0.02,+0.03}_{-0.02,-0.03}$	—	—
1000	100	10	$222^{+17,+18}_{-17,-14}$	$0.23^{+0.02,+0.04}_{-0.02,-0.03}$	—	—
1000	100	1000	$195^{+15,+17}_{-15,-13}$	$0.18^{+0.01,+0.03}_{-0.01,-0.02}$	—	—

$\sigma \times \mathcal{L}$	Mass [GeV]	$c\tau_0$ [mm]	1 Tag Obs	2 Tag Obs	3 Tag Obs	4 Tag Obs
100	700	10	205.14	23.05	20.45	11.89
100	700	1000	211.56	17.98	9.04	3.62
1000	100	10	403.57	74.33	20.97	5.13
1000	100	1000	320.64	22.92	3.60	0.39

Table 5.7: A summary of the size of the signal injected in the signal injection test (top). A summary of signal region yields in the 2,3, and 4 nominal displaced jet tag bins (middle) and the observed number of tags (bottom), as a function of the size of the signal contamination, for a signal injection test using a fixed signal point $m_X = 700$ GeV and $c\tau_0 = 10$ mm with varied signal yields. The no signal case is included as a reference to the predicted values without contamination. The test is normalized such that the sum of signal and background events stays fixed at the observed number of events passing the analysis event selection. The contamination fraction corresponds to the hypothetical fraction of signal events contained within the events passing the event selection.

Contam. Fraction	Signal σ [fb]		
0	0		
0.01%	30		
0.10%	290		
1.04%	3000		
9.47%	28000		
Contamination %	2 tag pred	3 tag pred	4 tag pred
0	$1.34^{+0.25}_{-0.17}$	-	-
0.01%	$1.34^{+0.25}_{-0.17}$	-	-
0.10%	1.67 ± 0.33	-	-
1.04%	$6.71^{+0.91}_{-0.82}$	-	-
9.47%	205.38 ± 15.21	1.37 ± 0.08	-
Contamination %	2 tag obs	3 tag obs	4 tag obs
0.00%	0	0	0
0.01%	19	16	10
0.10%	179	159	93
1.04%	1914	1520	943
9.47%	17632	14883	8775

Table 5.8: Summary of the systematic uncertainties. When the uncertainty depends on the specific features of the models (mass, lifetime and decay mode of the long-lived particle) a range is quoted, which refers to the computed uncertainty for $N_{\text{tags}} = 2$ events.

Signal systematic uncertainty	Effect on yield
H_T trigger inefficiency	5.0%
Jet p_t trigger inefficiency	5.0%
Trigger online tracking modeling	1.0–35.0%
Luminosity	2.7%
Acceptance due to PDF	1.0–6.0%
Displaced-jet tag variable modeling	1.0–30.0%

Table 5.9: The predicted and observed number of events as a function of N_{tags} . The prediction is based on the mistagging probability derived from events with fewer than two tags. The full event selection is applied. The quoted uncertainty corresponds to the total background systematic uncertainty.

N_{tags}	Expected	Observed
2	$1.09^{+0.16}_{-0.15}$	1
≥ 3	$(4.9 \pm 1.0) \times 10^{-4}$	0

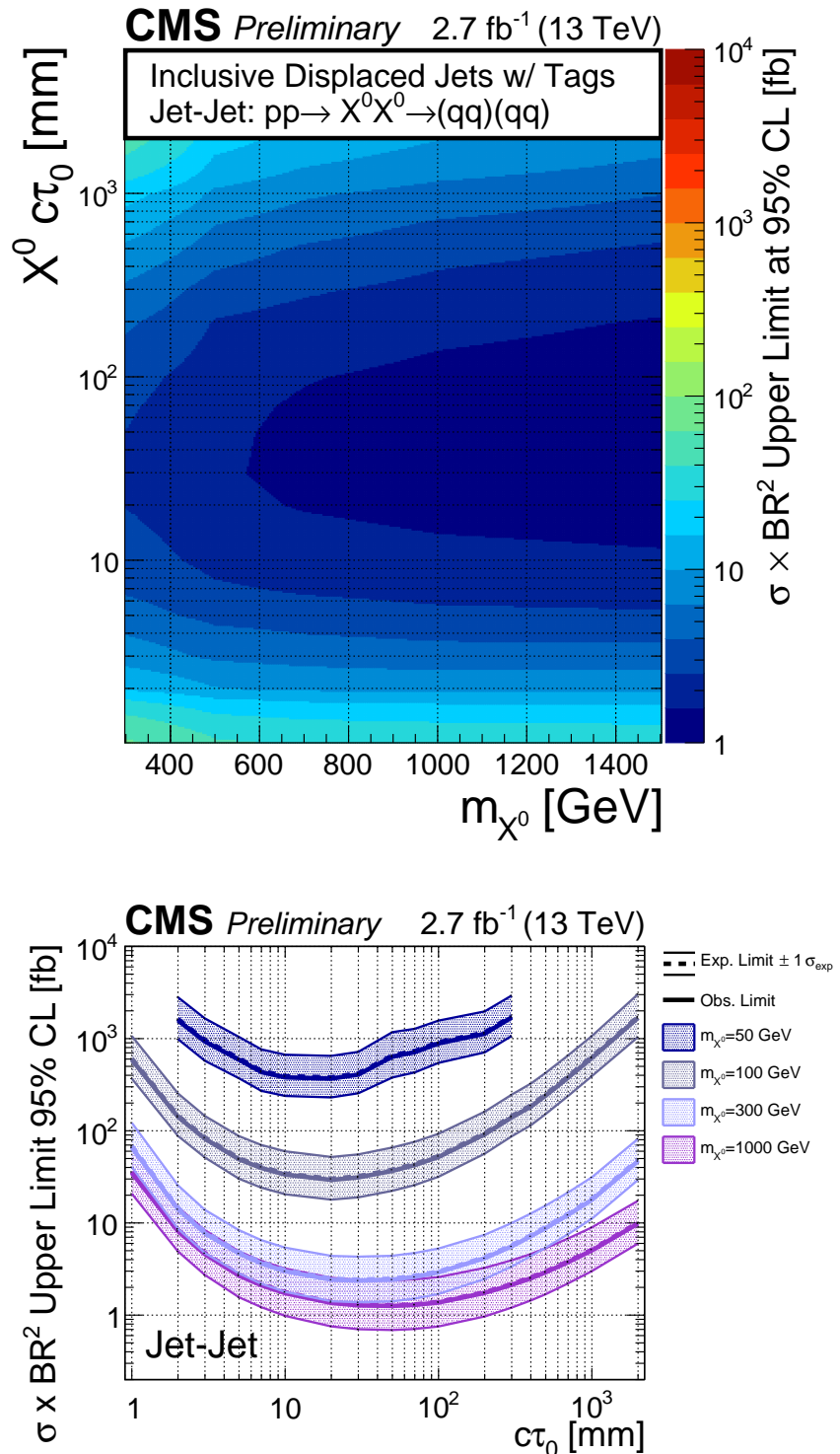


Figure 5.14: The excluded cross section at 95% CL for the Jet-Jet model as a function of the mass and lifetime of the parent particle X^0 (top) and as a function of the lifetime for four values of the mass (bottom).

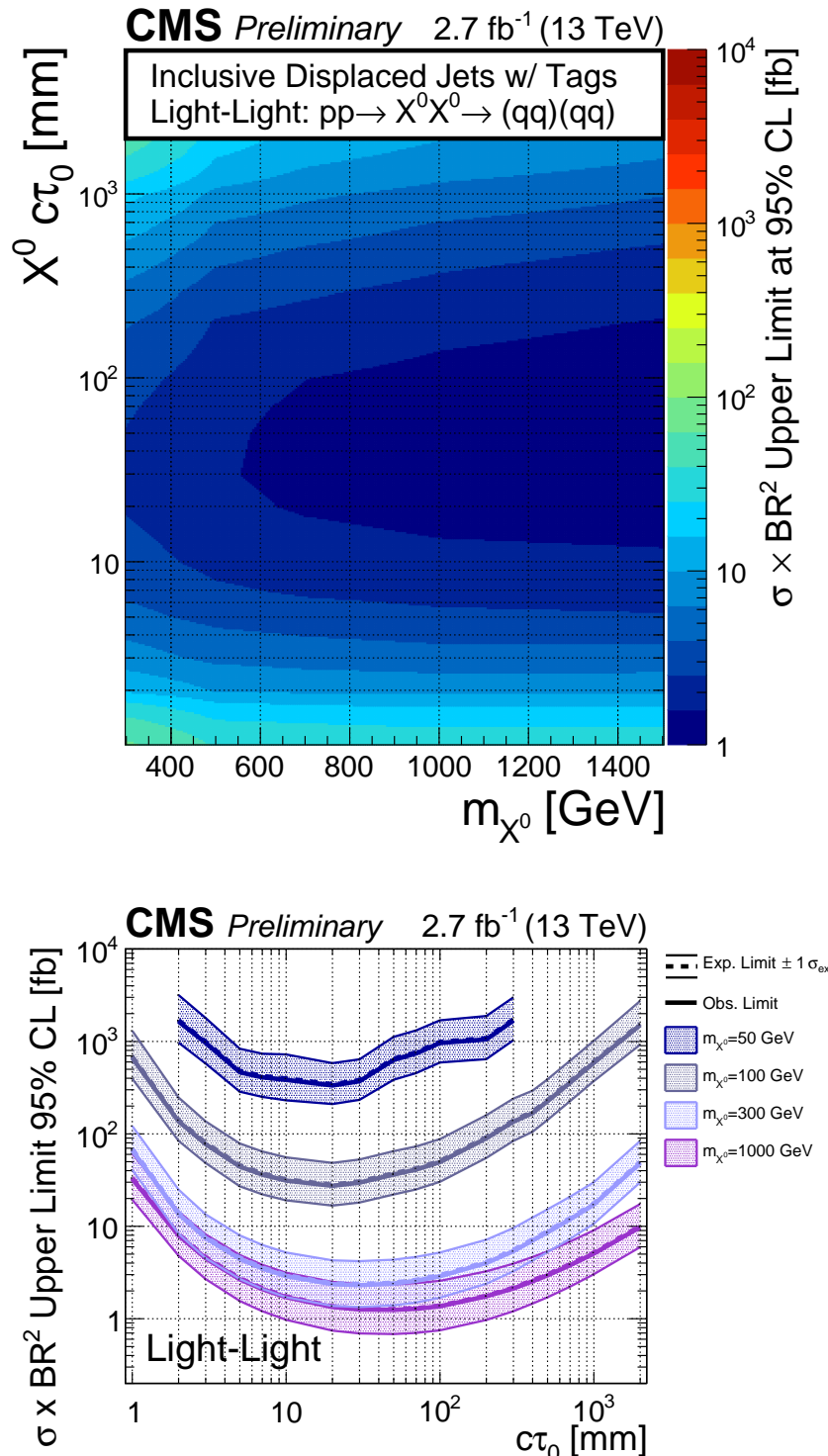


Figure 5.15: The excluded cross section at 95% CL for the Light-Light model as a function of the mass and lifetime of the parent particle X^0 (top) and as a function of the lifetime for four values of the mass (bottom).

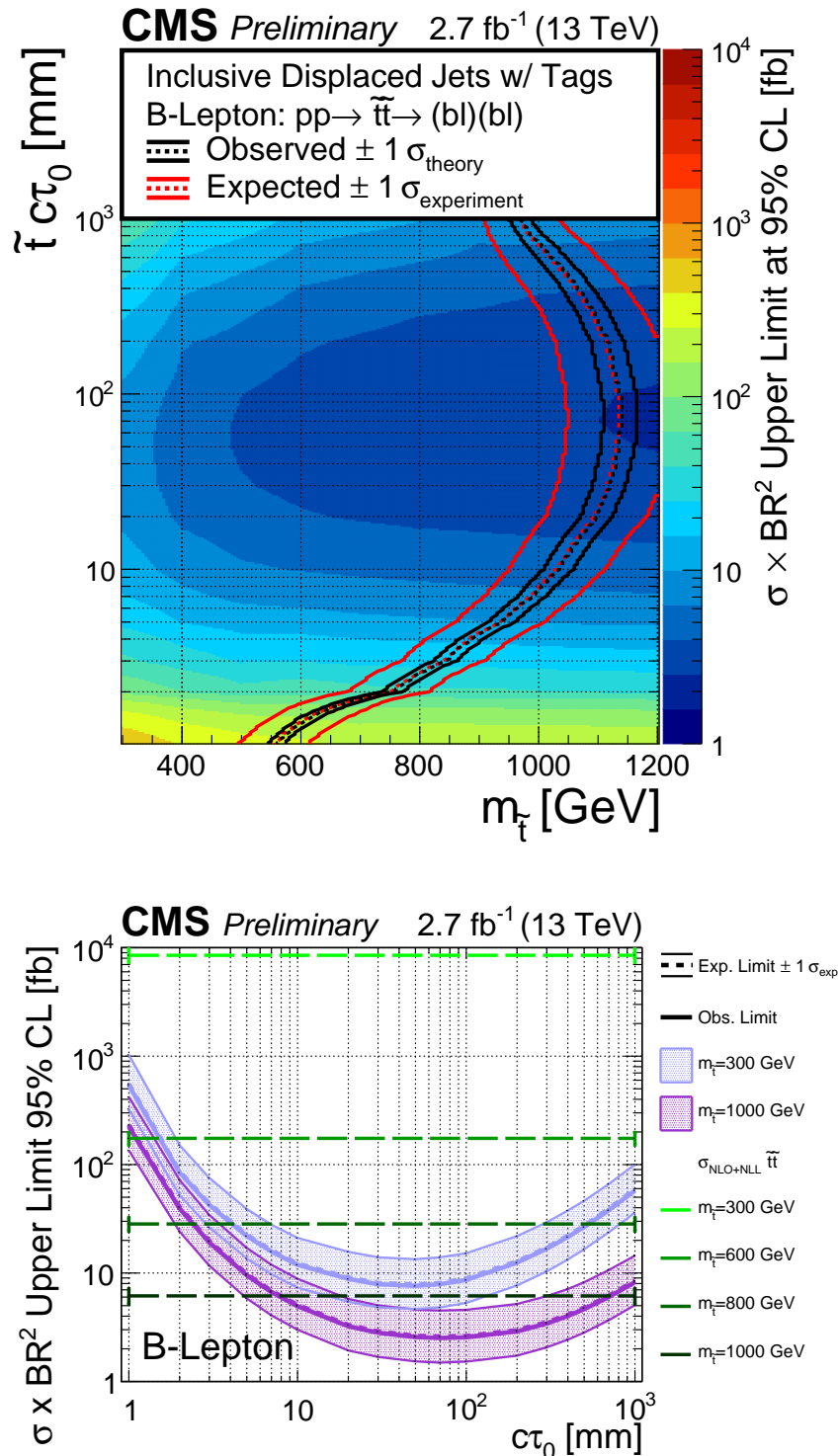


Figure 5.16: The excluded cross section at 95% CL for the B-Lepton model as a function of the mass and lifetime of the parent particle \tilde{t} (top) and as a function of the lifetime for two values of the mass (bottom). The bottom plot also shows the expected upper limits with one standard deviation uncertainties.

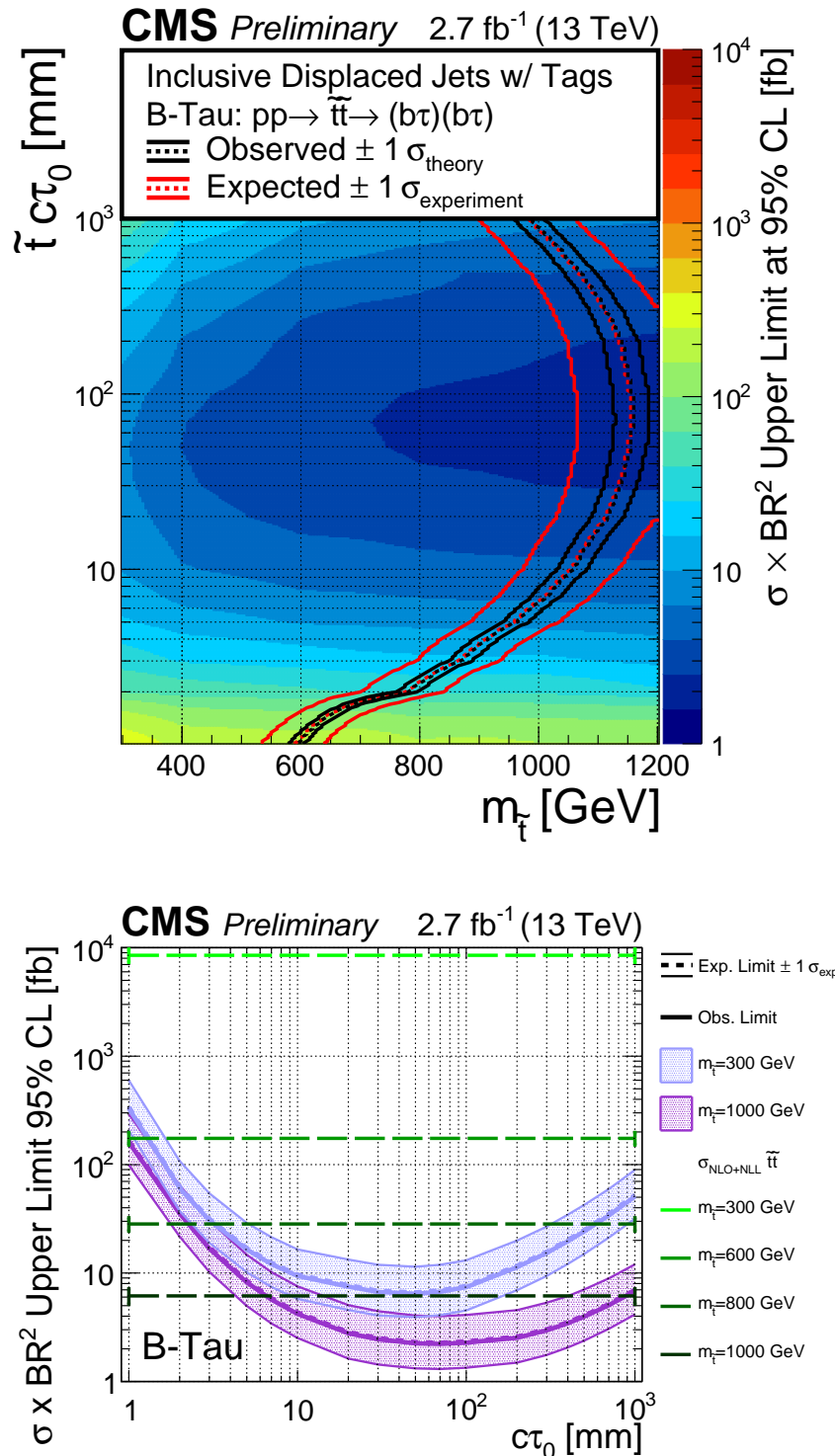


Figure 5.17: The excluded cross section at 95% CL for the B-Tau model as a function of the mass and lifetime of the parent particle \tilde{t} (top) and as a function of the lifetime for two values of the mass (bottom). The bottom plot also shows the expected upper limits with one standard deviation uncertainties.

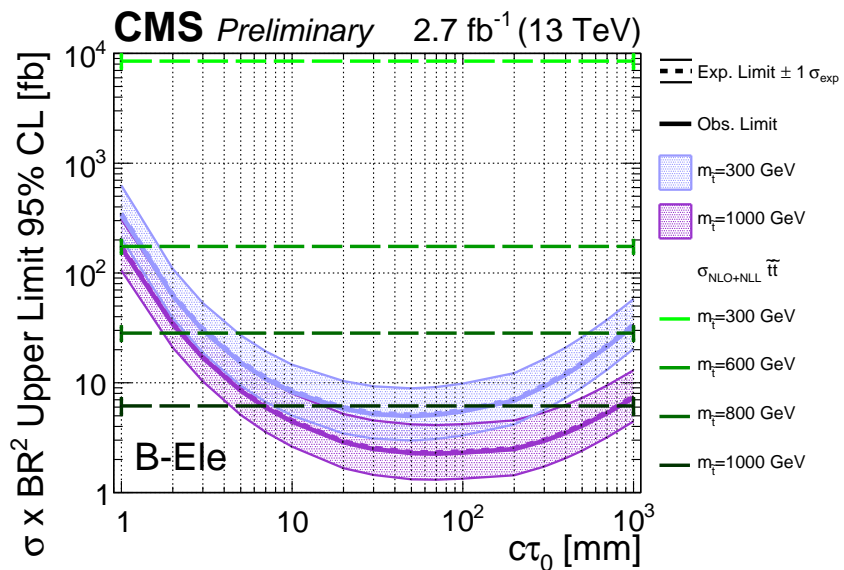
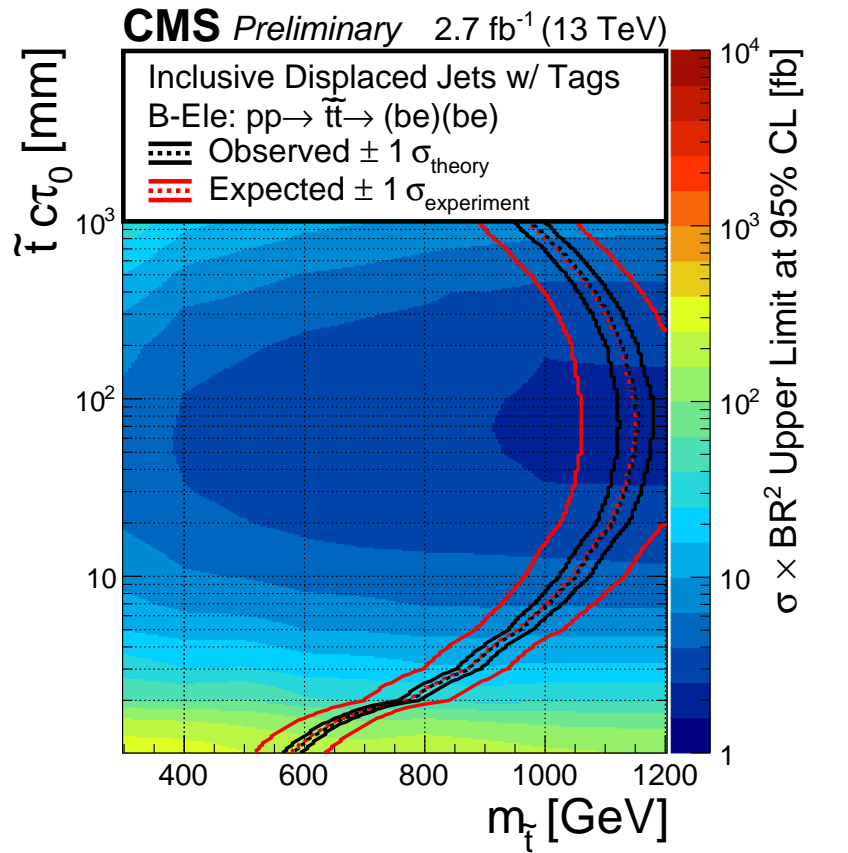


Figure 5.18: The excluded cross section at 95% CL for the B-Ele model as a function of the mass and lifetime of the parent particle \tilde{t} (top) and as a function of the lifetime for four values of the mass (bottom). The bottom plot also shows the expected upper limits with one standard deviation uncertainties.

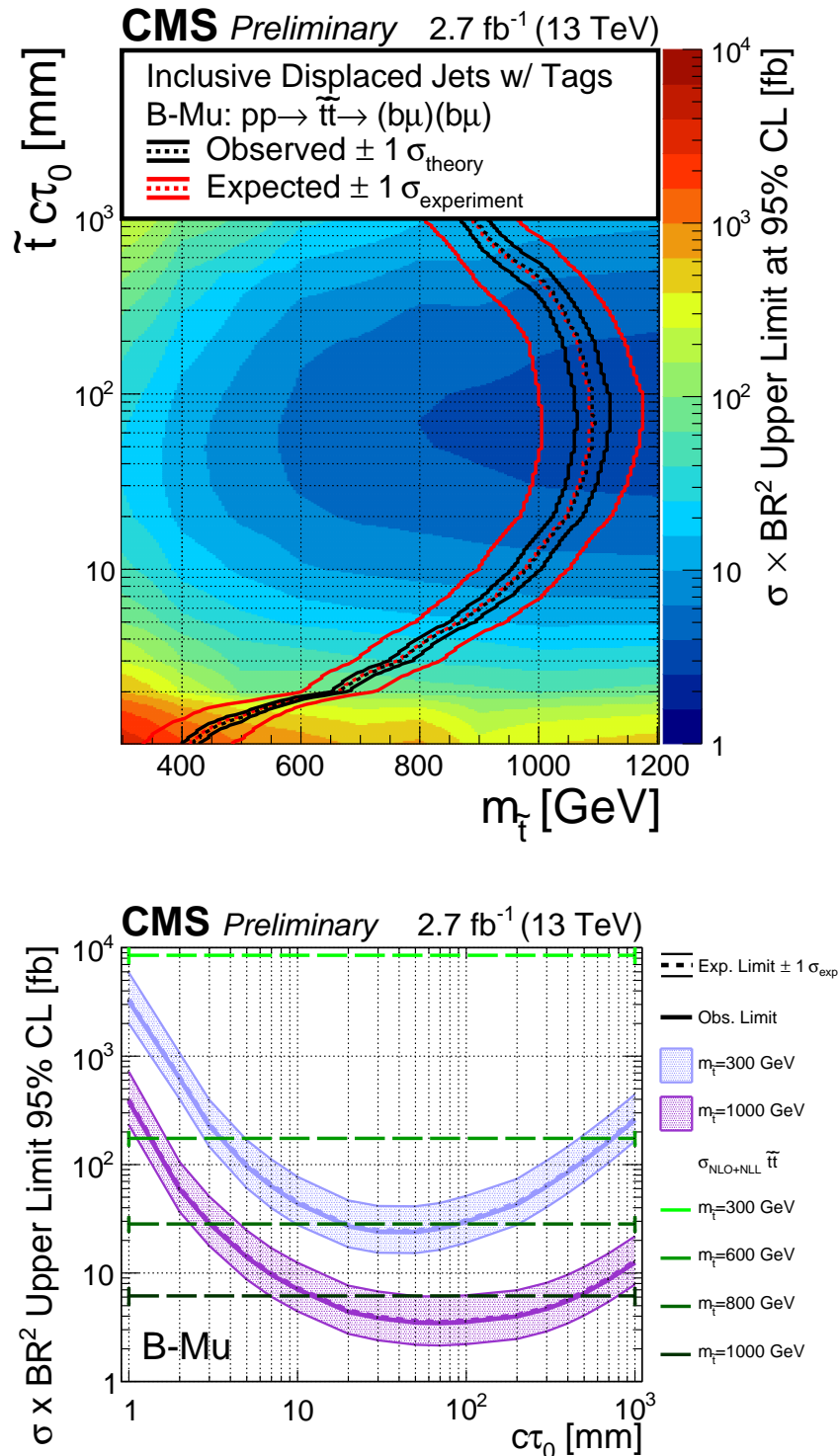


Figure 5.19: The excluded cross section at 95% CL for the B-Mu model as a function of the mass and lifetime of the parent particle \tilde{t} (top) and as a function of the lifetime for four values of the mass (bottom). The bottom plot also shows the expected upper limits with one standard deviation uncertainties.

Bibliography

- [1] J. Dalton. *A New System of Chemical Philosophy*. Manchester, 1808.
- [2] Georges Aad et al. Search for long-lived, weakly interacting particles that decay to displaced hadronic jets in proton-proton collisions at $\sqrt{s} = 8$ TeV with the atlas detector. *Phys. Rev. D*, 92:012010, 2015.
- [3] Georges Aad et al. Search for massive, long-lived particles using multitrack displaced vertices or displaced lepton pairs in pp collisions at $\sqrt{s} = 8$ TeV with the ATLAS detector. *Phys. Rev. D*, 92:072004, 2015.
- [4] Vardan Khachatryan et al. Search for Long-Lived Neutral Particles Decaying to Quark-Antiquark Pairs in Proton-Proton Collisions at $\sqrt{s} = 8$ TeV. *Phys. Rev. D*, 91:012007, 2015.
- [5] Matteo Cacciari, Gavin P. Salam, and Gregory Soyez. Fastjet user manual. *Eur. Phys. J. C*, 72, 2012.
- [6] Matteo Cacciari, Gavin P. Salam, and Gregory Soyez. The anti- k_t jet clustering algorithm. *JHEP*, 04:063, 2008.
- [7] T. Sjöstrand, Stephen Mrenna, and Peter Z. Skands. A brief introduction to PYTHIA 8.1. *Comput. Phys. Commun.*, 178:852, 2008.
- [8] R. et al Ball. Parton distributions with LHC data. *Nucl. Phys. B*, 867:244, 2013.
- [9] M. Strassler and Zurek K. Discovering the higgs through highly displaced vertices. *Phys. Lett. B*, 263, 2008.
- [10] P. Graham, D. Kaplan, S. Rajendran, and P. Sarawat. Displaced supersymmetry. *Journal of High Energy Physics*, 149, 2012.
- [11] CMS Luminosity Measurement for the 2015 Data Taking Period. Technical Report CMS-PAS-LUM-15-001, CERN, Geneva, 2016.
- [12] A. L. Read. Presentation of search results: the CL_s technique. *J. Phys. G*, 28:2693, 2002.
- [13] Thomas Junk. Confidence level computation for combining searches with small statistics. *Nucl. Instrum. Meth. A*, 434:435, 1999.

- [14] CMS and ATLAS Collaborations. Procedure for the lhc higgs boson search combination in summer 2011. CMS-NOTE-2011-005, 2011.
- [15] W. Beenakker, R. Höpker, M. Spira, and P. M. Zerwas. Squark and gluino production at hadron colliders. *Nucl. Phys. B*, 492:51, 1997.
- [16] A. Kulesza and L. Motyka. Threshold resummation for squark-antisquark and gluino-pair production at the LHC. *Phys. Rev. Lett.*, 102:111802, 2009.
- [17] A. Kulesza and L. Motyka. Soft gluon resummation for the production of gluino-gluino and squark-antisquark pairs at the LHC. *Phys. Rev. D*, 80:095004, 2009.
- [18] W. Beenakker, S. Brensing, M. Krämer, A. Kulesza, E. Laenen, and I. Niessen. Soft-gluon resummation for squark and gluino hadroproduction. *JHEP*, 12:041, 2009.
- [19] W. Beenakker, S. Brensing, M. Krämer, A. Kulesza, E. Laenen, L. Motyka, and I. Niessen. Squark and gluino hadroproduction. *Int. J. Mod. Phys. A*, 26:2637, 2011.
- [20] M. Krämer, A. Kulesza, R. van der Leeuw, M. Mangano, S. Padhi, T. Plehn, and X. Portell. Supersymmetry production cross sections in pp collisions at $\sqrt{s} = 7$ TeV. 2012.